Journal of Sound and Vibration 329 (2010) 2851–2872

Contents lists available at ScienceDirect

Journal of Sound and Vibration

journal homepage: www.elsevier.com/locate/jsvi

Finite element simulation of wave propagation in an axisymmetric bar

A.V. Idesman [a,*], K. Subramanian [a], M. Schmidt [b], J.R. Foley [b], Y. Tu [b], R.L. Sierakowski [b]

[a] Department of Mechanical Engineering, Texas Tech University, Lubbock, TX 79409-1021, USA
[b] Air Force Research Laboratory, Munitions Directorate, Eglin Air Force Base, FL 32542, USA

ARTICLE INFO

Article history:
Received 23 July 2009
Received in revised form
23 December 2009
Accepted 18 January 2010
Handling Editor: M.P. Cartmell
Available online 10 February 2010

ABSTRACT

An accurate solution for high-frequency pulse propagation in an axisymmetric elastic bar is obtained using a new finite element technique that yields accurate non-oscillatory solutions for wave propagation problems in solids. The solution of the problem is very important for the understanding of dynamics experiments in the split Hopkinson pressure bar (SHPB). In contrast to known approaches, no additional assumptions are necessary for the accurate solution of the considered problem. The new solution helps to elucidate the complicated distribution of parameters during high-frequency pulse propagation down the bar as well as to estimate the applicability of the traditional dispersion correction used in the literature for the analysis of wave propagation in a finite bar. Due to the dimensionless formulation of the problem, the numerical results obtained depend on Poisson's ratio, the length of the bar and the pulse frequency, and are independent of Young's modulus, the density and the radius of the bar.

1. Introduction

The current study is motivated by the analysis of velocity, strain and stress distributions in the split Hopkinson pressure bar (SHPB). Since its introduction in 1949 by Kolsky [1], the SHPB has been widely used for determining mechanical properties of different materials at high rates of loading. This technique is based on the theory of wave propagation in elastic bars. Despite the simple geometry of bars, there is no exact analytical solution for propagation of arbitrary pulses down a bar. The accurate description of high-frequency pulse propagation in the SHPB is an issue. Currently the Pochhammer–Chree solution for an infinitely long bar (the axisymmetric formulation) is used for the prediction of high-frequency stress and velocity pulse propagation in the SHPB. According to this solution, for wave propagation in an infinitely long cylinder, dependence (dispersion) exists between the pulse frequency and the wave velocity. The traditional dispersion correction for finite bars (e.g., see [2–13] and others) is based on the dispersion equation for an infinite cylinder. However, the application of the traditional dispersion correction to a finite cylinder with arbitrary boundary conditions has not been mathematically proved.

Other analytical and semi-analytical methods for the modeling of wave propagation in semi-infinite or finite bodies have been used in [14–21] and are based on integral transform techniques. However, these methods are difficult to apply

* Corresponding author.
E-mail address: alexander.idesman@coe.ttu.edu (A.V. Idesman).

0022-460X/$ - see front matter © 2010 Elsevier Ltd. All rights reserved.
doi:10.1016/j.jsv.2010.01.021

to wave propagation problems with arbitrary initial and boundary conditions even for a simple geometry. We should also mention that the recent solution derived in [21] for impact loading of an axisymmetric cylinder contains spurious oscillations due to Gibbs phenomena (see Section 3.1 and Fig. 4).

Another approach to the solution of wave propagation in a finite bar is based on the application of known numerical methods for elastodynamics to the considered problem; see [22–28] and others. Especially, the finite element method is very popular due to the simplicity of its application by the use of commercial finite element codes [23–28]. However, existing numerical approaches also do not allow an accurate solution of wave propagation problems due to large spurious high-frequency oscillations. Let us analyze the issues with existing numerical methods for elastodynamics in greater detail. Most finite element procedures for elastodynamics problems are based upon semi-discrete methods [29–35]. For these methods, the application of finite elements in space to linear elastodynamics problems leads to a system of ordinary differential equations in time

$$\mathbf{M}\ddot{\mathbf{U}}+\mathbf{C}\dot{\mathbf{U}}+\mathbf{K}\mathbf{U}=\mathbf{R}. \tag{1}$$

Here $\mathbf{M}$, $\mathbf{C}$, $\mathbf{K}$ are the mass, damping, and stiffness matrices, respectively, $\mathbf{U}$ is the vector of the nodal displacement, $\mathbf{R}$ is the vector of the nodal load. Eq. (1) can be also obtained by the application of other discretization methods in space such as the finite difference method, the spectral element method, the boundary element method, the smoothed particle hydrodynamics (SPH) method and others. Many different numerical methods have been developed for the time integration of Eq. (1). However, for wave propagation problems, the integration of Eq. (1) leads to the appearance of spurious high-frequency oscillations. Both the spatial discretization used for the derivation of Eq. (1), and the time integration of Eq. (1) affect spurious oscillations and the accuracy of a numerical solution. Even the exact time integration of Eq. (1) may yield very inaccurate solutions of the original (before the space discretization) system of elastodynamics equations due to large spurious high-frequency oscillations. This means that the integration of Eq. (1) with $\mathbf{C}=\mathbf{0}$ by a time integration method (with or without numerical dissipation) with very small time increments yields the numerical results that may be very inaccurate due to spurious oscillations. Moreover, mesh refinement and small time increments can lead to divergent results (e.g., see Fig. 6). In contrast to finite element solutions for linear static problems that converge to exact solutions at mesh refinement, the finite element solutions for linear elastodynamics may diverge at mesh refinement and very small time increments. Therefore, the treatment of spurious oscillations is crucial for obtaining accurate numerical results.

Current numerical approaches that treat this issue are based on the introduction of numerical dissipation or artificial viscosity from the first time increment for the suppression of spurious high-frequency oscillations. However, numerical dissipation or artificial viscosity also affects low modes of a numerical solution. Although this effect is small for a small number of time increments, due to error accumulation during the time integration of Eq. (1), low modes of numerical solutions become very inaccurate even at a moderate number of time increments. If numerical dissipation is not used in calculations, then spurious high-frequency oscillations spoil the numerical solution. We should also mention that the selection of the size of time increments as well as the amount of numerical dissipation or artificial viscosity is also an issue for integration of Eq. (1) related to wave propagation in solids. Usually, these parameters are user defined and are subjective because the accurate calibration of spurious oscillations is lacking. Another issue with numerical dissipation or artificial viscosity consists in the fact that the existing methods with numerical dissipation or artificial viscosity do not take into account the effect of the observation time (or the number of time increments) on the accuracy of final numerical results. Therefore, different researchers report different values of artificial viscosity needed for the suppression of spurious oscillations (e.g., see the recent paper [36] and references there), and it is not clear what the optimal value of artificial viscosity is or how to select it (there is no understanding that this value depends on the observation time). *The contradiction between the accuracy of low modes and the suppression of spurious high-frequency oscillations at different observation times cannot be resolved within the existing numerical approaches based on the time integration of Eq.* (1).

Recently we suggested a new numerical technique that yields non-oscillatory, accurate and reliable solutions for wave propagation in solids; see [37,38,40]. The purpose of the paper is accurate numerical analysis of wave propagation in an axisymmetric bar by the use of the new numerical technique. With the new approach, there is no need for additional assumptions (such as application of the dispersion equation for an infinite bar to a finite bar, or the user-defined amount of artificial viscosity or numerical dissipation used in the existing numerical approaches; see above) to obtain an accurate solution to the considered problem. The new approach yields numerical results converging to exact solutions at mesh refinement. This is not trivial for elastodynamics problems, as explained above. The results obtained allow the better understanding of high-frequency pulse propagation in a bar. The paper includes a short description of the new numerical technique based on the new two-stage solution strategy for elastodynamics and the new first-order time-continuous Galerkin (TCG) method used for filtering spurious high-frequency oscillations; see [37,38,40]. Then, as benchmark problems for testing the new numerical approach, we show the accurate numerical solutions of 1-D and 2-D axisymmetric impact problems which are very challenging problems from a computational point of view. Finally, we consider the propagation of rectangular and sinusoidal velocity pulses of different frequencies through an axisymmetric long cylinder and analyze the results obtained. An accurate numerical solution to this problem with existing numerical methods is an issue due to long-term integration and spurious numerical oscillations.

2. A new two-stage numerical technique

With the help of the new two-stage solution strategy and the new TCG methods suggested in [37 – 40], we will resolve the seemingly irresolvable contradiction of existing numerical approaches related to filtering spurious oscillations. The main advantages of the new strategy are as follows. The new numerical technique: (a) allows the selection of the best time-integration method for basic computations from simple criteria (the most important one being the accuracy of the method); (b) includes post-processing for filtering spurious high-frequency oscillations, which requires little computation time compared to the stage of basic computations (a small number of time increments with the new implicit TCG method with large numerical dissipation is used for post-processing); (c) yields no error accumulation due to numerical dissipation (or artificial viscosity) at the stage of basic computations; (d) allows the calibration of spurious oscillations at different observation times (see [38,40]) and does not require any guesswork for the selection of numerical dissipation or artificial viscosity as do the existing approaches. Thus, the approach can be easily incorporated in computer codes and does not require interaction with users for the suppression of spurious high-frequency oscillations. Below we briefly describe the new solution strategy for elastodynamics. The description of the new implicit TCG method with large numerical dissipation that, according to the new strategy, is used for post-processing, is given in Appendix A (see [37,38,40] for a detailed description and the application of the new strategy and the new TCG time-integration methods).

The idea of the new two-stage strategy is very simple. Because for linear elastodynamics problems there is no interaction between different modes during time integration (they are integrated independently of each other; see [37,38,40]), the most accurate time-integration method (usually without numerical dissipation or artificial viscosity) should be used for basic computations (the first stage), especially for a long-term integration. It means that all modes (including high-frequency modes) are integrated very accurately and the solution will include spurious high-frequency oscillations. Then, for the damping out of high modes, a method with large numerical dissipation (or with artificial viscosity) is used for a number of time increments as a post-processor (the second stage). This method can be considered a filter of high modes. Usually, a small number of time increments is sufficient for the second stage, with negligible error accumulation at low modes (10 time increments is used with the proposed technique; see [38]). Summarizing, in contrast to existing approaches with one time integration method, the new technique is based on the application of two different time integration methods to Eq. (1): one method is used for accurate integration of a semi-discrete system at the stage of basic computations and allows spurious oscillations; the other method is used for filtering spurious oscillations at the post-processing stage.

In the current paper, we will use the fourth-order explicit TCG method suggested in [41] for basic computations in order to obtain an accurate solution of the semi-discrete elastodynamics problem, Eq. (1) (this solution contains spurious high-frequency oscillations). We should mention that known methods such as the explicit central difference method or the implicit trapezoidal rule (the second-order time-integration methods with zero numerical dissipation) can also be used for basic computations with very small time increments. The selection of the high-order method for basic computations is related to the reduction of computation time compared to that required for second-order time-integration methods at the same accuracy. For filtering spurious oscillations, the new implicit TCG method with large numerical dissipation developed in [38,40] and briefly described in Appendix A is used. The proposed procedure has features in common with the modal decomposition method [42,43]. If all modes are used in the modal decomposition method, then the modal decomposition method yields the same results as the accurate time integration of a semi-discrete system Eq. (1) does. However, it is known that accurate numerical results can be obtained by the modal decomposition with a limited number of low modes. The application of numerical dissipation for post-processing in the suggested procedure is partly equivalent to removing a number of high modes from the numerical results for which all modes are included. It means that the new approach is partly equivalent to the modal decomposition method (without the necessity of calculations of the eigenvalues and eigenvectors of a semi-discrete system, Eq. (1)). At mesh refinement the new technique includes more modes in numerical solutions (because the decrease in Δx_j leads in the decrease in Δt and numerical dissipation; see Eqs. (A.6)–(A.8)), excludes spurious high modes, and converges to exact solutions. It also means that for actual high frequencies in applied loading a fine mesh that resolves these frequencies should be used.

3. Numerical modeling

The new technique based on the new two-stage solution strategy and the new TCG methods is implemented into the finite element code FEAP [35].

In [38,40] we showed that the new approach yields accurate non-oscillatory convergent results for 1-D impact and wave propagation problems for which the analytical solutions exist. Here, axisymmetric problems related to wave propagation in a bar are considered. First, the impact of a bar against a rigid wall is solved for the 1-D and 2-D cases using the new technique. Comparing the numerical solutions to these impact problems with the known solutions, we show the effectiveness of the new numerical technique. Then we apply the new technique to the problem of propagation of sinusoidal velocity pulses of different frequencies along a bar. As was shown in [38,40], at the same numbers of degrees of freedom, meshes with quadratic finite elements yield more accurate results for wave propagation problems than meshes with linear elements do. Therefore, for all calculations, axisymmetric quadratic 9-node finite elements are used.

3.1. Impact of an elastic bar against a rigid wall

First we show the application of the new numerical technique to the solution of the 1-D problem related to the impact of an elastic bar of the length L=4 against a rigid wall (see Fig. 1). Young's modulus is chosen to be E=1 and the density to be $\rho=1$. The following boundary conditions are applied: the displacement $u(0,t)=t$ (which corresponds to the velocity $v(0,t)= v_0 = 1$) and $u(4,t) = 0$ (which corresponds to the velocity $v(4,t)=0$). Initial displacements and velocities are zero; i.e., $u(x,0) = v(x,0)=0$. The problem has the continuous solution for displacements $u_a\ (x,t)= t - x$ for $t \geq x$ and $u_a\ (x,t)= 0$ for $t \leq x$, and the discontinuous solution for velocities and stresses $v_a(x,t) = -\sigma^a(x,t) = 1$ for $t \geq x$ and $v_a(x,t) = \sigma^a(x,t) = 0$ for $t \leq x$ (at the interface $x=t$, jumps in stresses and velocities occur). The observation time is chosen to be T=10. This time corresponds to reflection of a propagating wave from the right and left ends with the location of the wave front in the middle of the bar; see the analytical solution in Fig. 1 (curves 1). It was shown in [38] that the new solution strategy combined with the new first-order implicit TCG method yields an accurate and non-oscillatory solution to the 1-D impact problem considered. However, the detailed study related to the convergence of numerical results at mesh refinement has not been considered in [38].

The problem is solved on three uniform meshes with 100, 500 and 1000 quadratic 3-node elements. A consistent mass matrix is used in all calculations. The trapezoidal rule with uniform time increments $\Delta t = 0.0001$ is applied for basic computations. At time increments smaller than $\Delta t = 0.0001$, the numerical results do not practically differ from those obtained with $\Delta t = 0.0001$. The numerical results after basic computations include many spurious high-frequency oscillations in velocities on the coarse and fine meshes; see curves 2 and 3 in Fig. 1b and c. These oscillations spoil the numerical solutions and make them impractical (similar oscillatory numerical results for the 1-D impact problem can be found in [44–46] and others). Moreover, the amplitudes of spurious oscillations increase at mesh refinement; i.e., the numerical results are divergent at mesh refinement due to spurious oscillations (see curves 2 and 3 in Fig. 1b and c). In order to filter the spurious oscillations, post-processing with the implicit first-order TCG method using 10 uniform time increments (according to Eqs. (A.6)–(A.8), $\Delta t = 0.021$, $\Delta t = 0.00621$, and $\Delta t = 0.00366$ for meshes with 100, 500 and 1000 quadratic 3-node elements, respectively) is applied. Non-oscillatory smooth results are obtained after post-processing; see curves 2–4 in Fig. 1d. Fig. 1d also shows that the non-oscillatory numerical results, obtained with the new numerical

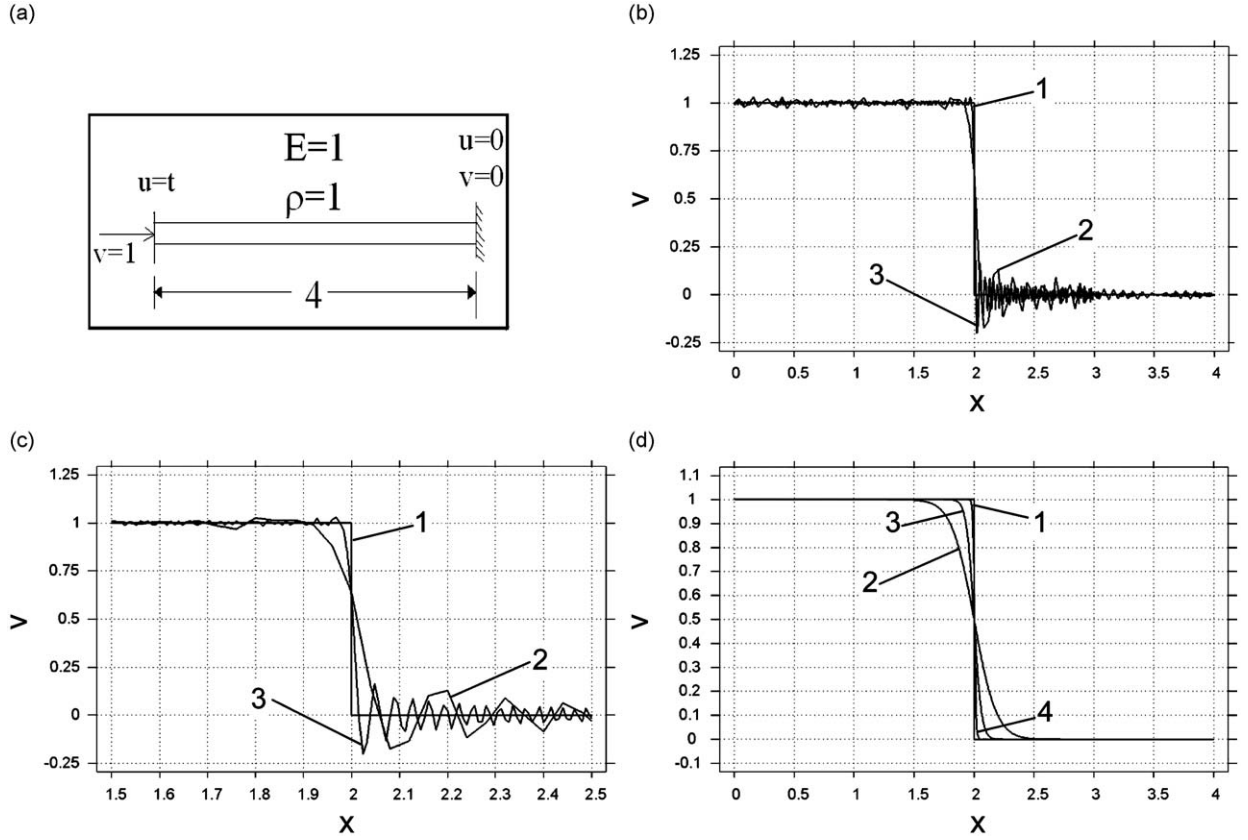

Fig. 1. Impact of an elastic bar of length L=4 against a rigid wall (a). Velocity distribution along the bar at observation times T=10 after basic computations (b, c) and after post-processing (d). Curves 1 correspond to the analytical solution. Curves 2, 3 and 4 correspond to the solutions calculated on uniform meshes with 100, 500 and 1000 quadratic 3-node finite elements, respectively. (c) The zoomed graph (b) in the range $1.5 < x < 2.5$.

technique (basic computations plus post-processing) converge to the analytical solution at mesh refinement. The 1-D impact problem with propagating discontinuities in stresses and velocities can be considered a good benchmark problem for the testing of new numerical methods for wave propagation problems.

3.2. Impact of an elastic cylinder against a rigid wall

A cylinder of length $L = 2.5$ and radius $R = 1$ is considered; see Fig. 2. The z-axis is the axis of revolution. Young's modulus is chosen to be $E=1$, Poisson's ratio $v=0.3$, and the density to be $\rho=1$. The following boundary conditions are applied: along boundary AB $u_n = t$ (which corresponds to the instantaneous application of velocity $v_n = v_0 = 1$) and $\tau_n=0$; along boundaries CD and AD $\sigma_n=0$ and $\tau_n=0$; along boundary BC $u_n = 0$ and $\tau_n=0$, where u_n, v_n, and σ_n are the normal displacements, velocities and the normal tractive forces, respectively; τ_n are the tangential tractive forces. Initial displacements and velocities are zero; i.e., $u_i(r,z,0)=v_i(r,z,0)=0$. To compare the numerical results obtained with the known solution derived in [21], the following dimensionless coordinates ($\bar{r}$ and $\bar{z}$), the dimensionless time $\bar{t}$

$$\bar{r}=\frac{r}{R},\quad \bar{z}=\frac{z}{R},\quad \bar{t}=\frac{tc_0}{R} \tag{2}$$

and the normalized displacements $\bar{u}_i$, velocities $\bar{v}_i$, stresses $\bar{\sigma}_{ij}$ and strains $\bar{\varepsilon}_{ij}$

$$\bar{u}_i=\frac{u_i c_0}{Rv_0},\quad \bar{v}_i=\frac{v_i}{v_0},\quad \bar{\varepsilon}_{ij}=\frac{\varepsilon_{ij}c_0}{v_0},$$

$$\bar{\sigma}_{ij}=\frac{\sigma_{ij}c_0\sqrt{(1+v)(1-v)(1-2v)}}{vEv_0},\quad i,j=r,z \tag{3}$$

are used, where $c_0=\sqrt{E/\rho}$ is the longitudinal wave rate in the 1-D case. The dimensionless observation time is chosen to be $\bar{T}=1.724$. The problem was solved on three uniform meshes with $50\times100=5000$, $100\times200=20\,000$ and $200\times400=80\,000$ quadratic 9-node elements. A consistent mass matrix was used in all calculations. The trapezoidal rule with uniform time increments $\Delta\bar{t}=0.000479$ was applied for basic computations. At time increments smaller than $\Delta\bar{t}=0.000479$, the numerical results do not practically differ from those obtained with $\Delta\bar{t}=0.000479$. It means that at $\Delta\bar{t}=0.000479$ the error in time is small and the numerical solution is close to the exact solution of a semi-discrete system, Eq. (1). The application of the new explicit fourth-order TCG method (see [41]) with uniform time increments $\Delta\bar{t}=0.000479$ yielded practically the same results for basic computations. The numerical results after basic computations include many spurious high-frequency oscillations in stresses and velocities on the coarse and fine meshes; see curves 1 in Fig. 3. These oscillations spoil the numerical solution and make it impractical. Then, in order to filter the oscillations, post-processing with the implicit first-order TCG method using 10 uniform time increments (according to Eqs. (A.6)–(A.8), $\Delta\bar{t}=0.0141$, $\Delta\bar{t}=0.0083$, and $\Delta\bar{t}=0.0049$ for meshes with $50\times100=5000$, $100\times200=20\,000$ and $200\times400=80\,000$ quadratic 9-node elements, respectively) was applied. Non-oscillatory smooth results were obtained after post-processing; see curves 2 in Figs. 3 and 4.

Remark. The size of time increments of the implicit first-order TCG method with large numerical dissipation, that is used for post-processing, depends on finite element dimensions, material properties and observation time, and is selected according to the formula suggested in [38,40]; see also Eqs. (A.6)–(A.8). As was shown in [38,40], at the selected time increments (the size of time increments indirectly prescribes the minimum amount of numerical dissipation needed for filtering spurious high-frequency oscillations), spurious high-frequency oscillations are damped out for uniform finite element meshes at any observation time.

Fig. 4 shows the convergence of non-oscillatory numerical results, obtained with the new numerical technique (basic computations plus post-processing) at mesh refinement, to the approximation of the analytical solution derived in [21] by the Laplace transform. The approximate analytical solution (curves 1 in Fig. 4) has spurious oscillations due to Gibbs

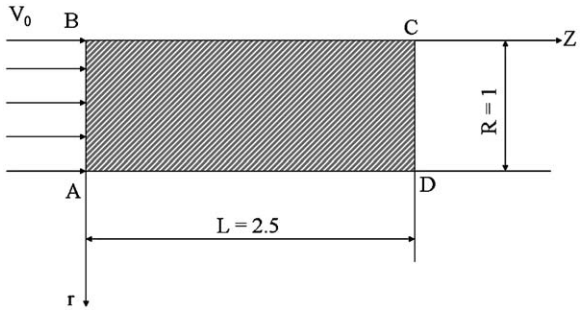

Fig. 2. Axisymmetric impact of an elastic cylinder of length L and radius R against a rigid wall. z is the axis of revolution.

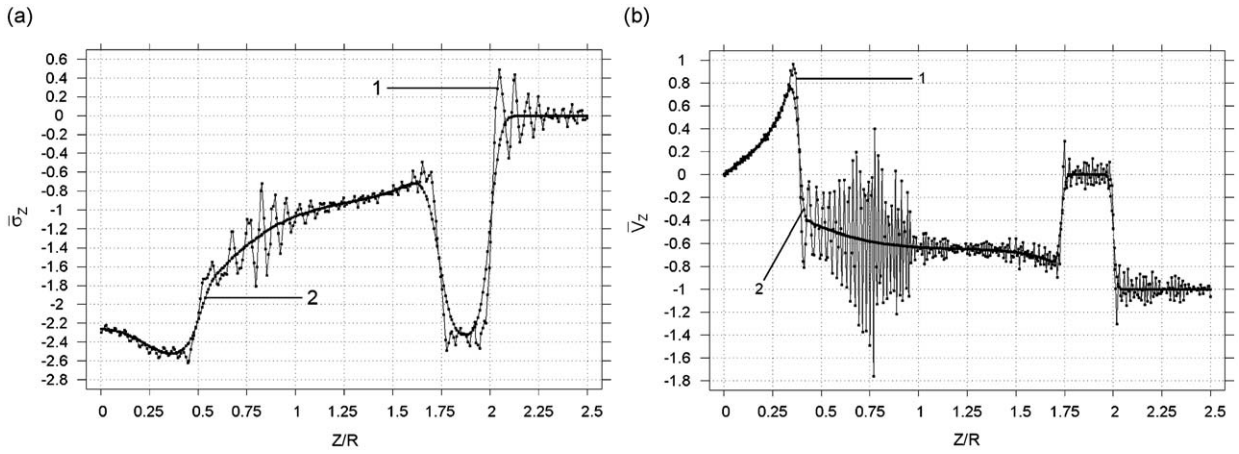

Fig. 3. The distribution of the dimensionless axial stress $\overline{\sigma}_z$ (a) and velocity $\overline{v}_z$ (b) along the dimensionless axial coordinate $\overline{z}=z/R$ and the fixed dimensionless radial coordinate $\overline{r}$ ($\overline{r}=0.05$ for (a) and $\overline{r}=0$ for (b)) at dimensionless time $\overline{T}=c_0t/R=1.724$. Curves 1 and 2 correspond to the numerical solutions obtained by the trapezoidal rule and by the subsequent post-processing, respectively. Uniform meshes with 5000 (a) and 80 000 (b) quadratic $Q9$ elements were used.

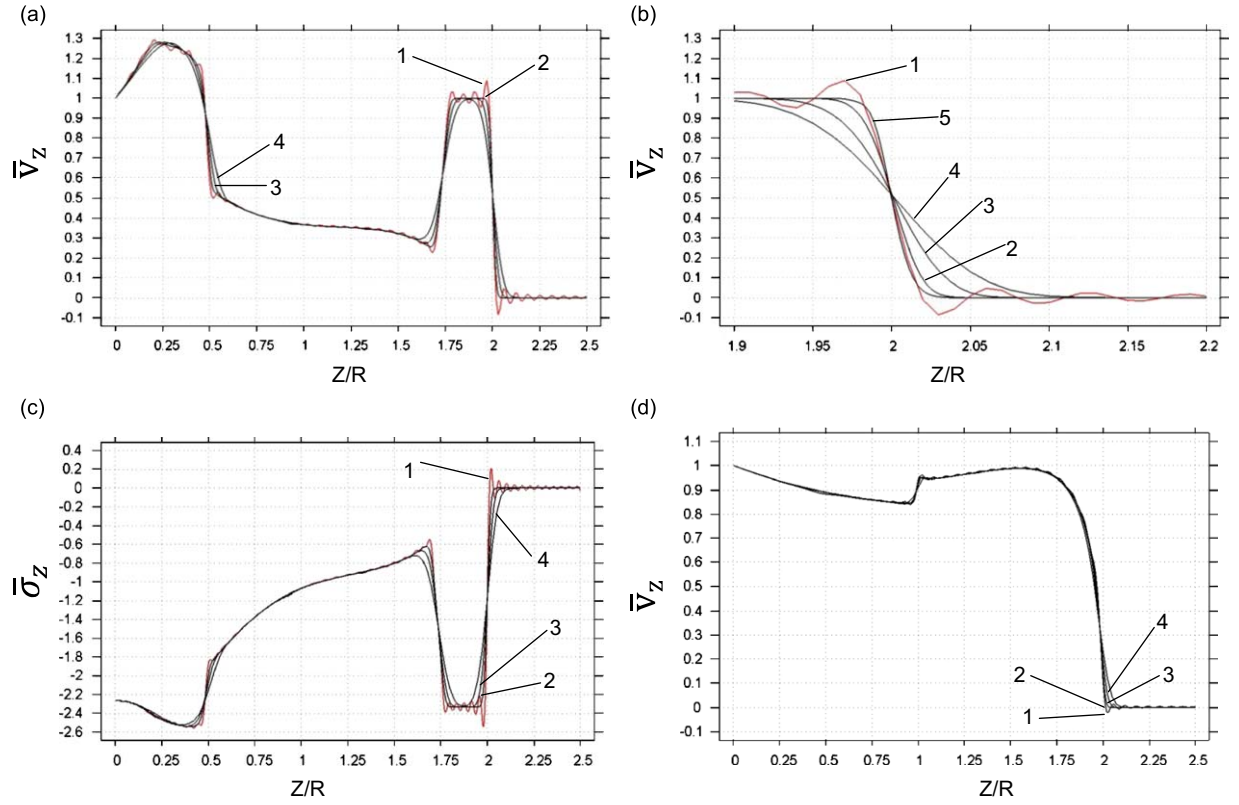

Fig. 4. The distribution of the dimensionless velocity $\overline{v}_z$ (a, b, d) and axial stress $\overline{\sigma}_z$ (c) along the dimensionless axial coordinate $\overline{z}=z/R$ and the fixed dimensionless radial coordinate $\overline{r}$ ($\overline{r}=0.05$ for (a), (b) and (c), and $\overline{r}=1$ for (d)) at dimensionless time $\overline{T}=c_0t/R=1.724$. Curves 1 correspond to the approximation of the analytical solution; see [21]. Curves 2, 3, 4 (a–d) and 5 (b) correspond to the numerical solutions obtained with the new solution strategy on uniform meshes with 80 000, 20 000, 5000, and 320 000 quadratic $Q9$ elements, respectively. (b) The zoomed graph (a) in the range $1.9<Z/R<2.2$.

phenomena. These oscillations can be clearly seen for the range $2<z/R<2.5$ in Fig. 4 where the exact stresses and velocities are zero (a non-disturbed domain). Fig. 4b shows in detail the velocity distribution in the vicinity of the wave front. This figure additionally includes the velocity obtained on a very fine mesh with $400\times800=320\,000$ quadratic

9-node elements. It can be seen that the wave front for the finest mesh (curve 5) does not contain spurious oscillations and is sharper than that for the approximate analytical solution (curve 1).

The numerical solution of the considered impact problem shows the effectiveness of the new numerical technique for wave propagation problems and can be considered a test for the next problems (see below), which differ from the impact problem by the boundary conditions and the length of the bar only.

3.3. Propagation of half-sinusoidal velocity pulses of different frequencies through an axisymmetric bar

Long cylinders are usually used for the SHPB, and a long cylinder of length $L = 50$ and radius $R = 1$ is considered; see Fig. 5. For the understanding of high-frequency pulse propagation in a cylinder, the simplest sinusoidal velocity pulses of different frequencies are applied, and their propagation down the bar is studied. The following boundary conditions are applied: along boundary AB $u_n = v_0[1-\cos(2\pi ft)/(2\pi f)]$ (which corresponds to the sinusoidal velocity pulse $v_n = v_0\sin(2\pi ft)$) and $\tau_n = 0$ for $t \le t_1$, and $\sigma_n = 0$ and $\tau_n = 0$ for $t \ge t_1$; along boundaries CD and AD $\sigma_n = 0$ and $\tau_n = 0$; along boundary BC $u_n = 0$ and $\tau_n = 0$, where f is the frequency of the pulse, v_0 is the amplitude of the pulse, the duration of the pulse t_1 is selected as $t_1 = 0.5/f$ (it corresponds to half-sinusoidal velocity pulses), u_n, v_n, and σ_n are the normal displacements, velocities and the normal tractive forces, respectively; τ_n are the tangential tractive forces. Initial displacements and velocities are zero; i.e., $u_i(r,z,0)=v_i(r,z,0)=0$. To generalize the numerical results obtained, the dimensionless coordinates ($\overline{r}$ and $\overline{z}$) and the dimensionless time $\overline{t}$ given by Eq. (2), and the normalized displacements $\overline{u}_i$, velocities $\overline{v}_i$, stresses $\overline{\sigma}_{ij}$ and strains $\overline{\varepsilon}_{ij}$ given by Eq. (3) are used. In this case, for linear elastic isotropic materials, numerical results are independent of Young's modulus, the density, the amplitude of the velocity v_0 and the radius of the cylinder (in calculations we use $E=1$, $\rho = 1$, $v_0=1$), and depend on Poisson's ratio, the frequency of the pulse, and the length of the cylinder; i.e.

$$\overline{u}_i = \overline{u}_i(\overline{r},\overline{z},\overline{t},f,v,L), \quad \overline{v}_i = \overline{v}_i(\overline{r},\overline{z},\overline{t},f,v,L),$$

$$\overline{\varepsilon}_{ij} = \overline{\varepsilon}_{ij}(\overline{r},\overline{z},\overline{t},f,v,L), \quad \overline{\sigma}_{ij} = \overline{\sigma}_{ij}(\overline{r},\overline{z},\overline{t},f,v,L). \tag{4}$$

Remark. Until the wave front reaches the right end of the cylinder, the numerical results are independent of the length of the bar as well.

The case of Poisson's ratio $v = 0.3$ and four different frequencies $f = 0.025c_0/R; 0.1c_0/R; 0.25c_0/R; 0.5c_0/R$ is studied. The selected material properties correspond to the following dimensionless longitudinal $\overline{c}_1 = c_1/c_0 = \sqrt{(1-v)/((1+v)(1-2v))} = 1.1602$ and transversal $\overline{c}_2 = c_2/c_0 = \sqrt{1/(2(1+v))} = 0.6202$ waves in an unbounded isotropic continuum. The maximum dimensionless observation time is chosen to be $\overline{T} = 100$. During this time all pulses travel from the left end of the cylinder to the right end and back from the right end to the location close to the left end (the reflected wave). The problem is solved on three uniform meshes with $10 \times 500 = 5000$ (42 042 degrees of freedom), $20 \times 1000 = 20\,000$ (164 082 degrees of freedom) and $40 \times 2000 = 80\,000$ (648 162 degrees of freedom) quadratic 9-node elements. A consistent mass matrix is used in all calculations. The new explicit fourth-order TCG method (see [41]) with uniform time increments $\Delta\overline{t} = 0.0004$ is applied for basic computations. At these small time increments, the error in time is small and can be disregarded. We should mention that any known explicit or implicit time-integration method of second or higher orders of accuracy with relatively small time increments can be used at the stage of basic computation.

Numerical results are presented in Figs. 6–12. As we expect, the numerical results after basic computations include many spurious high-frequency oscillations on the coarse and fine meshes; e.g., see the velocity distribution for frequency $f = 0.25c_0/R$ at time $\overline{T} = \overline{t} = 40$ in Fig. 6. From Fig. 6 we can see that the amplitudes of spurious oscillations are much greater at the axis of revolution than those at the external surface of the cylinder. These oscillations spoil the numerical solution and make it impractical. Moreover, the numerical results do not converge at mesh refinement due to the increase in the amplitudes of spurious oscillations; see Fig. 6. Then, in order to filter the oscillations, post-processing with the

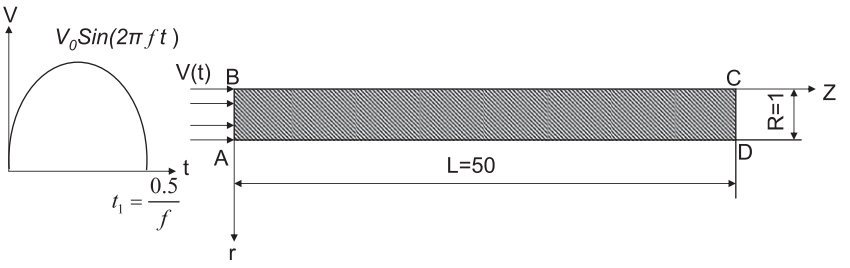

Fig. 5. Propagation of a sinusoidal pulse along a cylinder. z is the axis of revolution.

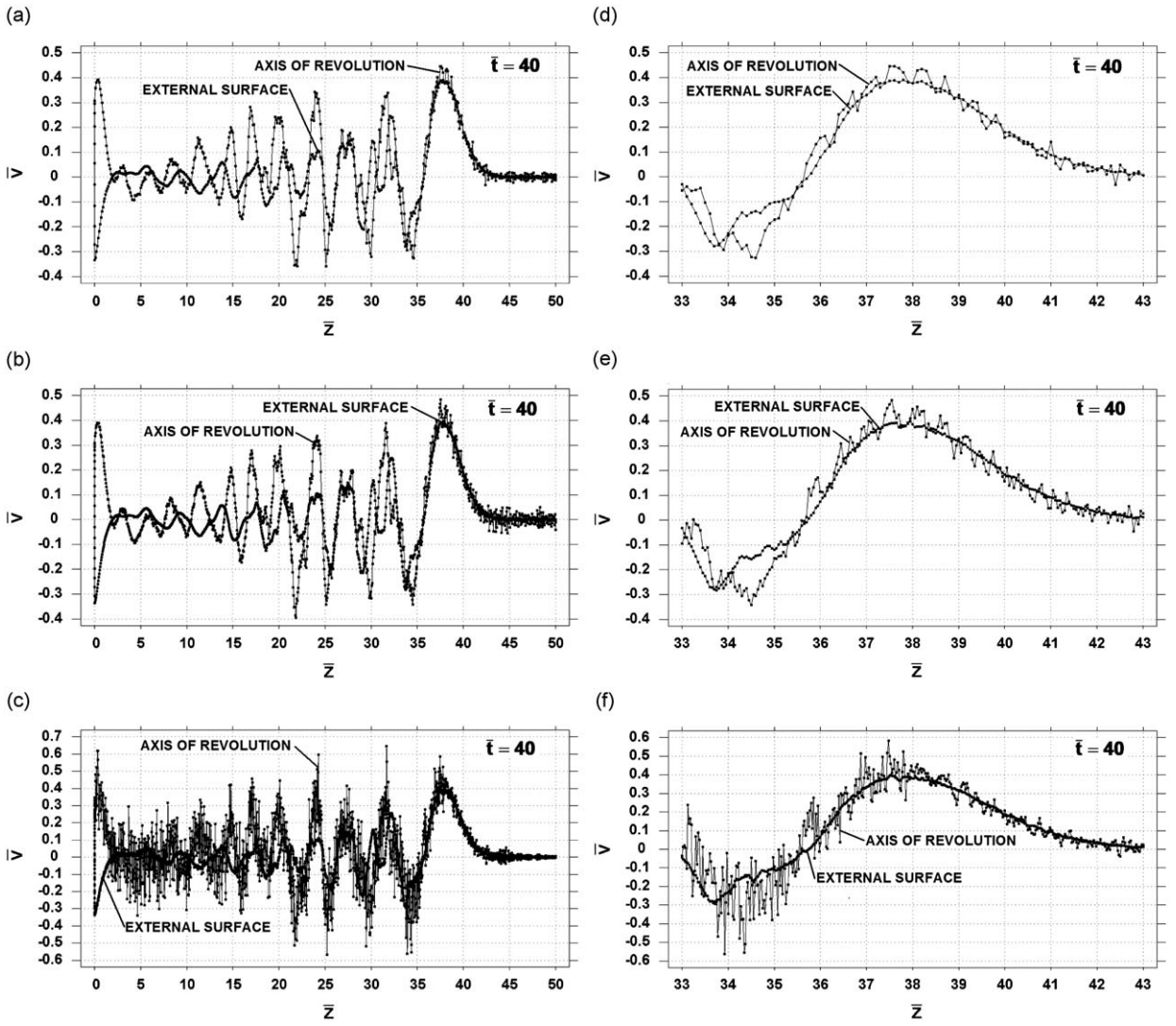

Fig. 6. Distribution of the axial velocity along the axis of revolution and along the axial line on the external surface at time $\bar{t} = 40$ after the basic calculations (no post-processing). The sinusoidal velocity pulse of frequency $f = 10f_1 = 0.25c_0/R$ is applied. (a, d), (b, e) and (c, f) correspond to the finite element meshes with 5000, 20 000 and 80 000 quadratic elements, respectively. (d–f) correspond to the zoomed graphs (a–c) in the range $33 \le \bar{z} \le 43$.

implicit first-order TCG method using 10 uniform time increments is applied (the size of time increments at different observation times is calculated according to Eqs. (A.6)–(A.8)). The accurate non-oscillatory results are obtained after post-processing; e.g., see the velocity distribution for the same frequency $f = 0.25c_0/R$ and at the same time $\bar{T} = 40$ in Fig. 7. The results in Fig. 7 also show that the fine mesh yields better resolution and captures some actual oscillations that cannot be resolved by the coarse mesh. Therefore, the numerical results for the frequencies $f = 0.5c_0/R; 0.25c_0/R; 0.1c_0/R$ are presented for the fine mesh with 80 000 elements; see Figs. 10–12. For the low frequency $f = 0.025c_0/R$, results on all three meshes are practically the same; i.e., a relatively coarse mesh can be used for low frequencies.

Let us compare and analyze the results related to propagation of the sinusoidal velocity pulses of different frequencies down the cylinder. The low-frequency pulse ($f = f_1 = 0.025c_0/R$) propagates with the velocity $c_0 = 1$; see Fig. 8. The changes in the shape and amplitude of the low-frequency pulse during its propagation down the bar, as well as the variation of the velocity over cross sections are insignificant (see Figs. 8 and 9); i.e., the 1-D theory for propagation of non-dispersive longitudinal waves in a bar is applicable in the case of low-frequency pulses. However, with the increase in frequency, the solution becomes much more complicated than that for low frequency (or for the 1-D case); see Figs. 9–12. The axial velocity is non-homogeneously distributed along the radius of the cylinder, and the difference between the velocity at the axis of revolution and at the external surface for the same cross section increases with the increase in the pulse frequency; see Figs. 10–12. The amplitude of the pulse decreases with the propagation of the pulse down the bar (the initial amplitudes of all four selected sinusoidal pulses are the same and equal unity), and the decrease becomes more essential

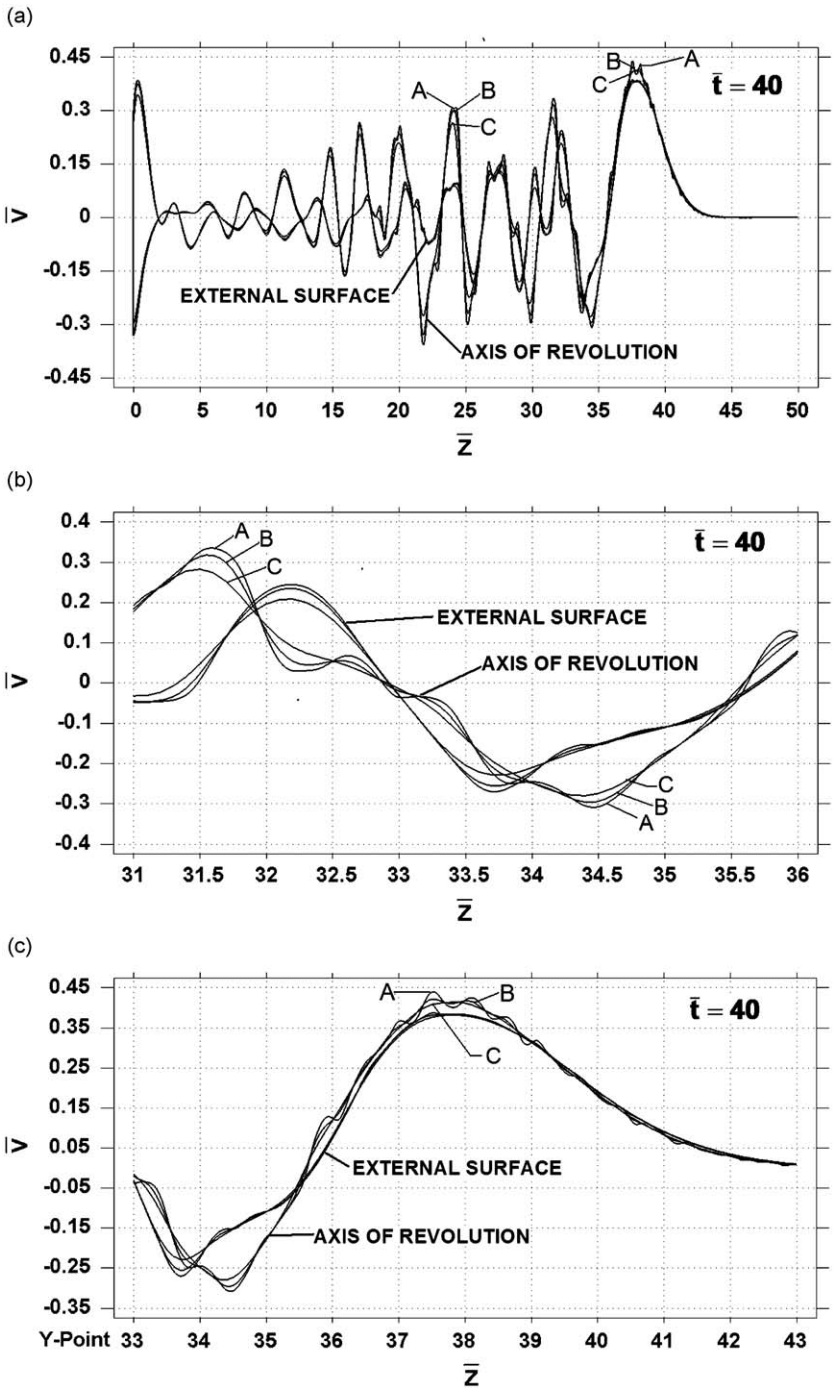

Fig. 7. Distribution of the axial velocity along the axis of revolution and along the axial line on the external surface at time $\bar{t} = 40$ after post-processing. The sinusoidal velocity pulse of frequency $f = 10f_1 = 0.25c_0/R$ is applied. A, B and C correspond to the finite element meshes with 80 000, 20 000 and 5000 quadratic elements, respectively. (b, c) correspond to the zoomed graph (a).

with the increase in frequency. High-frequency pulses excite vibrations behind the wave front and activate a broad range of frequencies of a cylinder. Figs. 10–12 show that short time after the pulse application the wave front of high-frequency pulses propagates with the velocity close to c_0 = 1, which corresponds to the longitudinal wave rate in the 1-D case. The results in Figs. 10–12 also show that the first oscillations behind the wave front mostly consists of low frequency components; i.e., the cylinder transforms high-frequency sinusoidal pulses into complicated pulses for which the first oscillation behind the wave front corresponds to low-frequency components; see the shapes of the pulses in the vicinity of

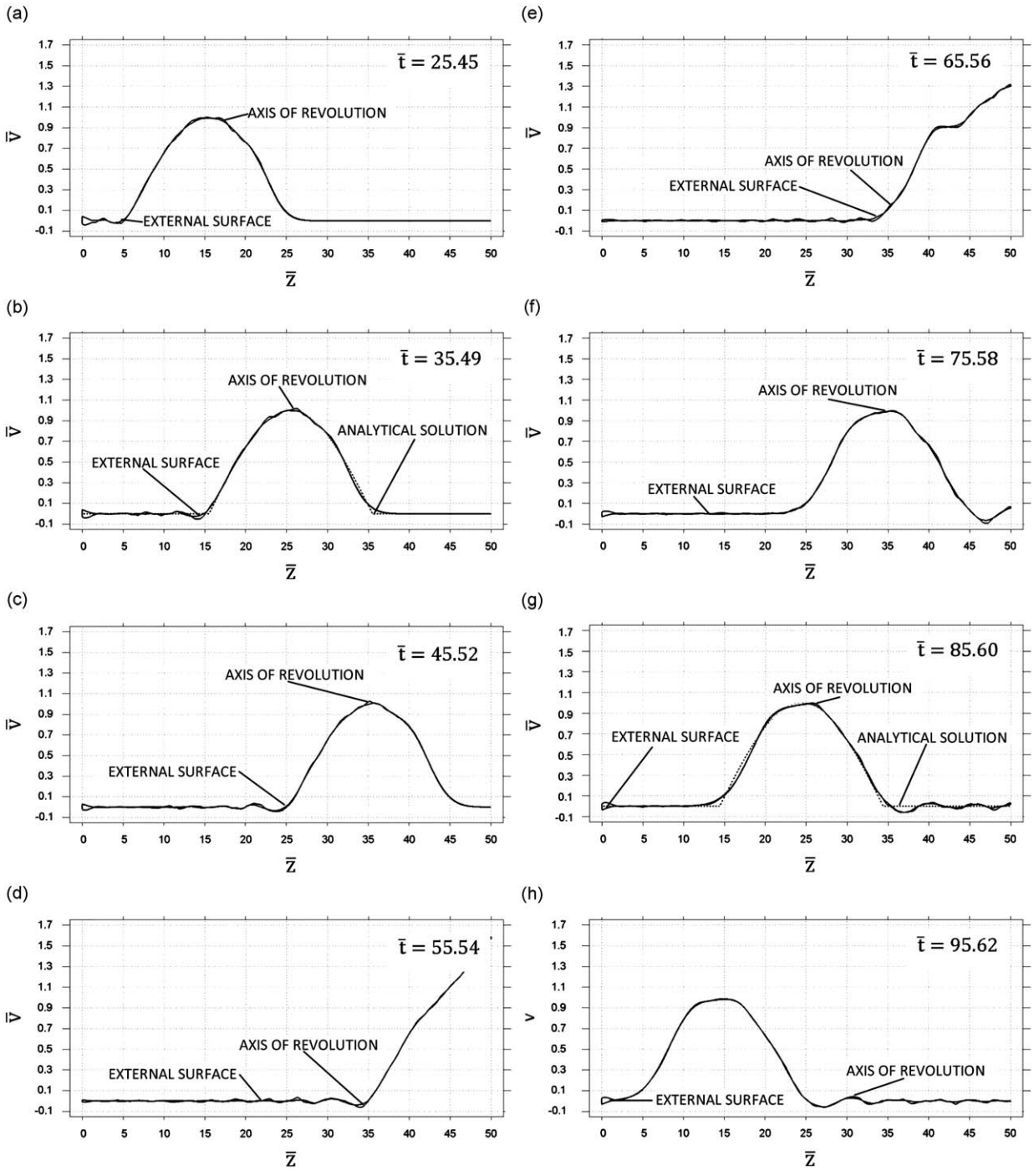

Fig. 8. Distribution of the axial velocity along the axis of revolution and along the axial line on the external surface at different times $\bar{t} = 25.45$ (a), 35.49 (b), 45.52 (c), 55.54 (d), 65.56 (e), 75.58 (f), 85.60 (g), 95.62 (h). The sinusoidal velocity pulse of frequency $f = f_1 = 0.025c_0/R$ is applied. Dash lines in (b, g) correspond to the analytical solution for the 1-D case.

the wave front. The results in Fig. 9 show that the variation of the axial velocity with respect to time at points with coordinates z=12.5; 25; 37.5 on the external surface of the cylinder (a parameter that can be measured in experiments) becomes much more complicated with the increase in pulse frequency. Due to this complicated time variation of the axial velocity for high-frequency pulses, it is difficult or impossible (see Figs. 9h,k and l) for high-frequency pulses to identify the wave front of the reflected pulse for points located at a great distance from the end where the pulse was applied.

Remark 1. The axial velocity of the wave front for an incident pulse can be calculated by the use of the locations of the wave front at different observation times found from the numerical solution. However, the velocity changes smoothly in the vicinity of the wave front from zero to non-zero values because the first oscillation behind the wave front corresponds to low-frequency components. Therefore the location of the wave fronts (the boundary between zero and non-zero

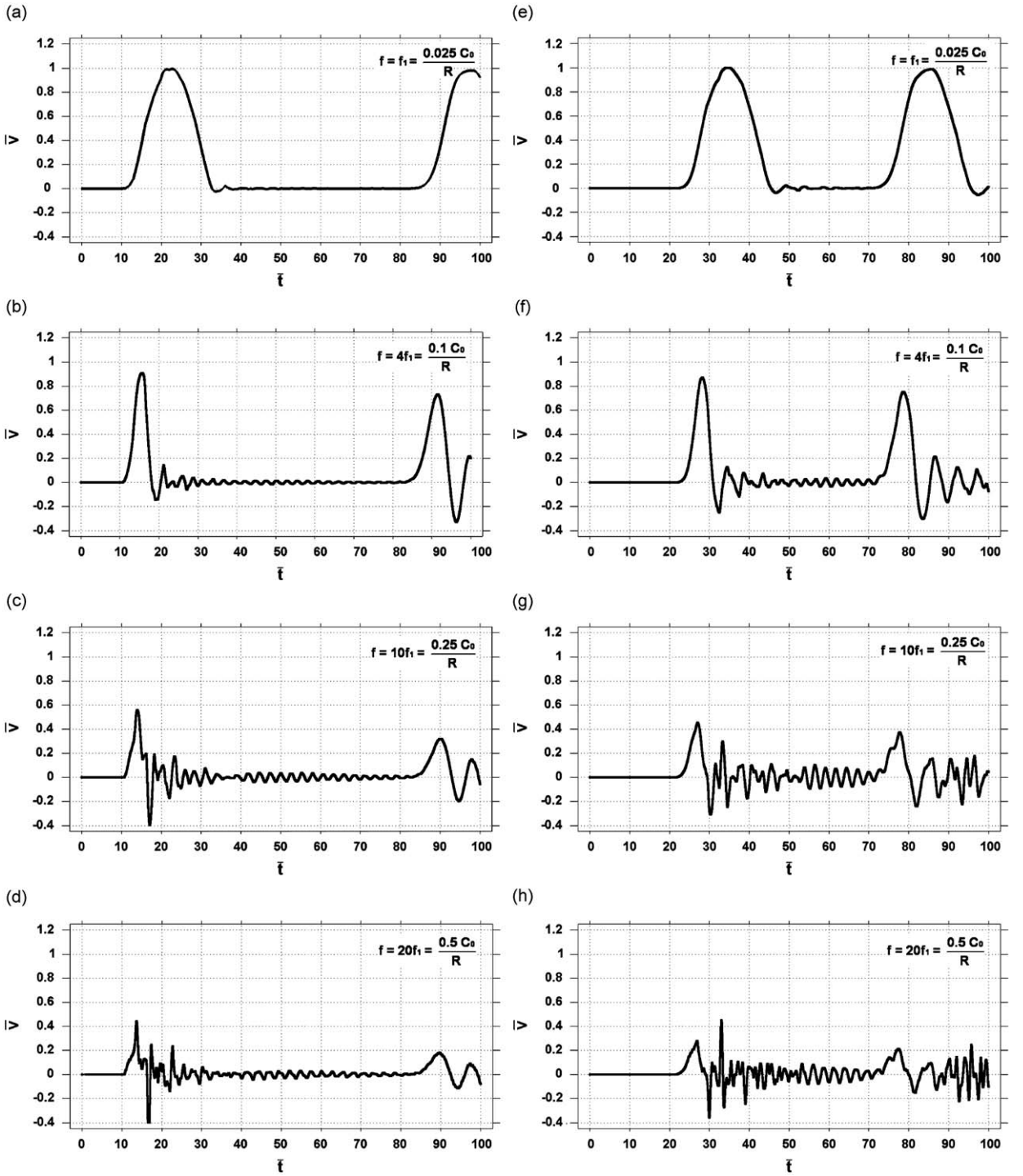

Fig. 9. Variation of the axial velocity in time at points with coordinates z=12.5 (a–d), z=25 (e–h), z=37.5 (i–l) on the external surface of the cylinder. (a,e,i), (b,f,j), (c,g,k) and (d,h,l) correspond to the sinusoidal velocity pulses of frequency $f = f_1 = 0.025c_0/R; 4f_1; 10f_1; 20f_1$, respectively.

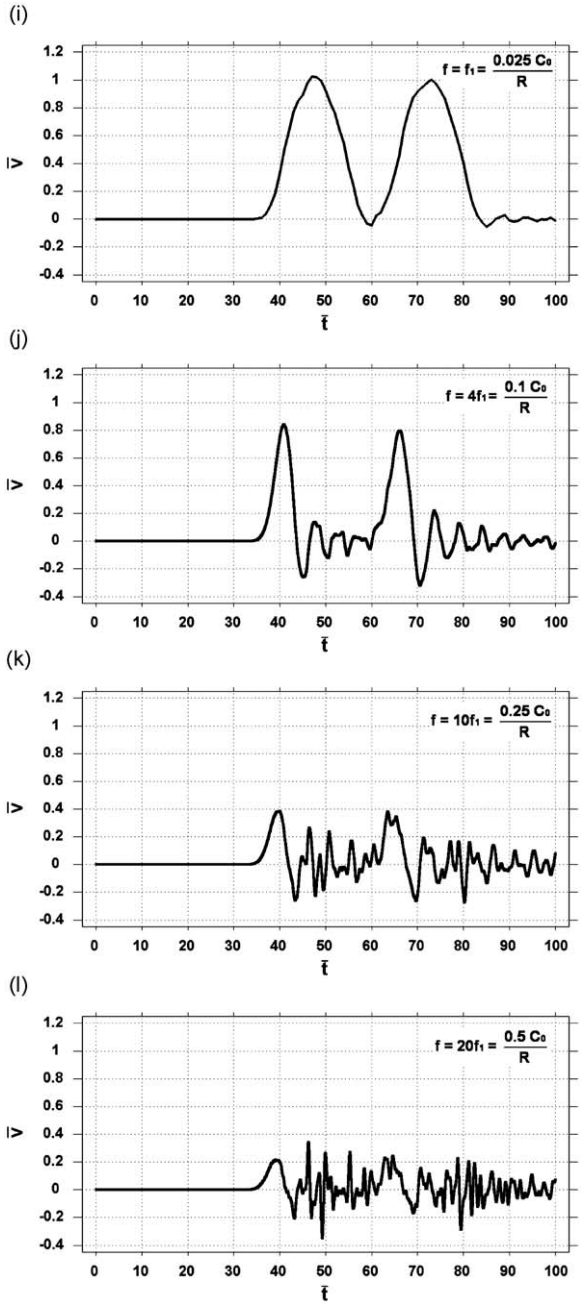

Fig. 9. (*Continued*)

velocities) at different observation times can be determined from the numerical solution with some error. In order to increase the accuracy in determination of the wave front velocity, we determine the location of the points behind the wave front corresponding to a small value of the velocity; e.g., $\overline{v}=0.025$. It means that in Figs. 10–12 we should find the intersection of the first oscillation behind the wave front and the horizontal line $\overline{v}=0.025$. These points can be determined much more accurately than the exact position of the wave front with zero velocity. Knowing the location of these points at different observation times, we can easily find the velocity of the wave front.

Remark 2. We should note that the difference between low- and high-frequency pulses propagating in the SHPB consists in the fact that in contrast to propagation of low-frequency pulses, propagation of high-frequency pulses cannot be described by the 1-D wave equation. Because waves in the 1-D case are non-dispersive and propagate with velocity c_0, one way to quantify the boundary between low- or high-frequency pulses propagating in the SHPB can be based

on the dispersion equation of the Pochhammer–Chree solution for an infinitely long bar. For example, the upper bound for low frequencies w^b can be introduced as the frequency w for which the phase velocity c for an infinite axisymmetric bar equals $(1-\varepsilon^{in})c_0$ where ε^{in} is the tolerance (e.g., $\varepsilon^{in}=0.01$). By the analysis of the first fundamental mode of the dispersion equation (e.g., see [47]), it follows that the phase velocities close to c_0 correspond to small values of kR where $k=w/c$ is the wave number. For small $kR<1$, the dispersion equation can be approximated by the following formula (e.g., see [47]):

$$c=c_0[1-\tfrac{1}{4}\nu^2k^2R^2]+O(kR)^4. \tag{5}$$

Then frequency w^b for an infinite circular bar can be found from Eq. (5) as follows:

$$c=(1-\varepsilon^{in})c_0\approx c_0\left[1-\frac{1}{4}\nu^2\left(\frac{w^b}{c_0}\right)^2R^2\right] \quad \text{or} \quad w^b=\frac{2\sqrt{\varepsilon^{in}}}{\nu}\frac{c_0}{R}. \tag{6}$$

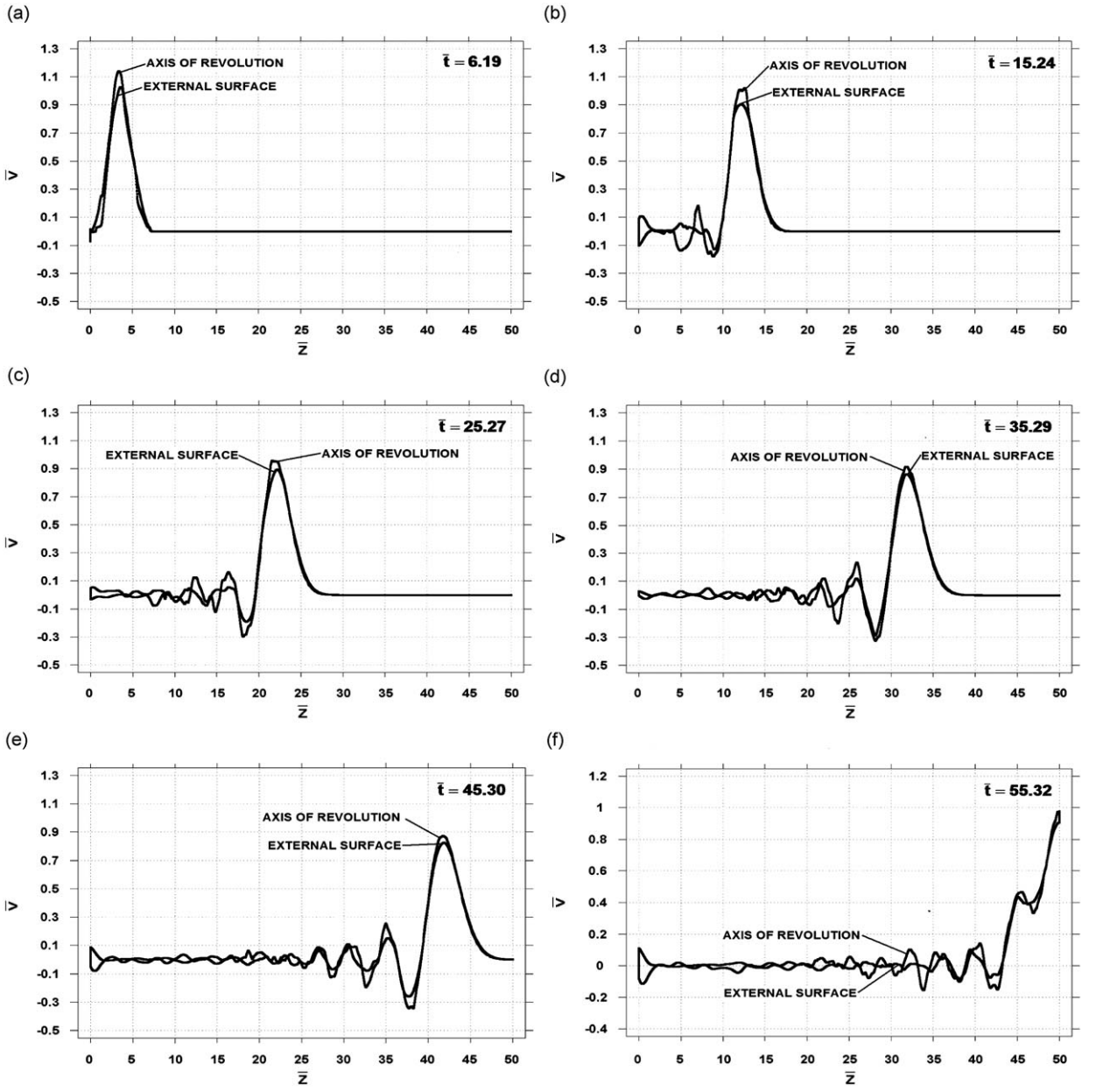

Fig. 10. Distribution of the axial velocity along the axis of revolution and along the axial line on the external surface at different instances $\bar{t}=6.19$ (a), 15.24 (b), 25.27 (c), 35.29 (d), 45.30 (e), 55.32 (f), 65.33 (g), 75.34 (h) and 80.35 (i). The sinusoidal velocity pulse of frequency $f=4f_1=0.1c_0/R$ is applied.

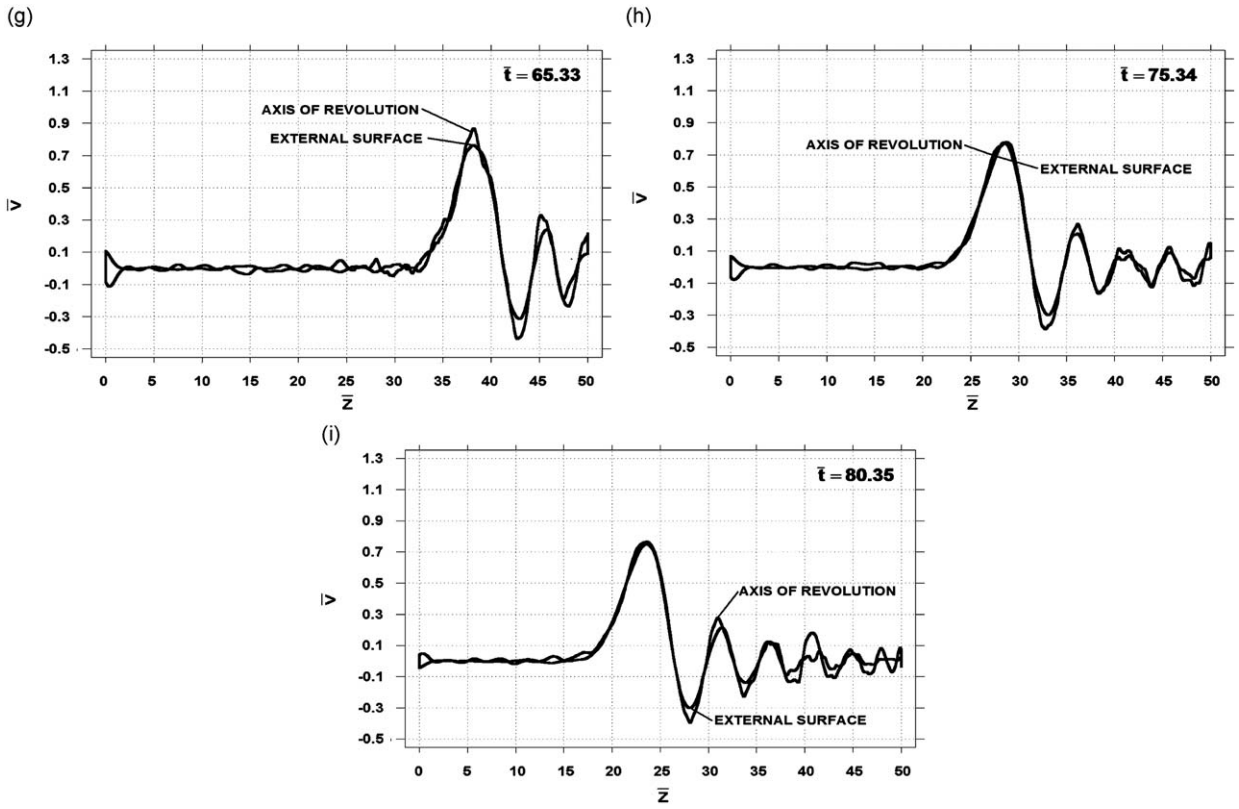

Fig. 10. (*Continued*)

However, accurate numerical solutions for wave propagation in a finite bar allow the quantification of low- and high-frequency pulses based on the comparison of the velocity distribution for the 1-D and 2-D axisymmetric wave propagation problems with given initial and boundary conditions. For example, comparing the axial velocity distributions from the numerical solution for an axisymmetric bar $\overline{v}$ (see Figs. 8–12) and from the 1-D analytical solution $\overline{v}_{1D}$ for propagation of the same applied pulse $v_n = v_0 \sin(2\pi f t)$ at the same observation time (e.g., $T = L/2c_0$ which corresponds to the dimensionless time $\overline{T} = L/2R$ and the position of the wave front in the middle of a bar), the following definition of the upper bound $\tilde{f}$ of low-frequency pulses can be introduced:

$$\max_{\overline{r},\overline{z}} |\overline{v}(\overline{r},\overline{z},\overline{T},\tilde{f},\nu) - \overline{v}_{1D}(\overline{r},\overline{T},\tilde{f})| = \varepsilon^{fi}, \tag{7}$$

where ε^{fi} is the tolerance (e.g., $\varepsilon^{fi} = 0.05$). It means that at given ν, ε^{fi} and $\overline{T} = L/2R$, the upper bound $\tilde{f}$ of low-frequency pulses can be found from Eq. (7) (for the dimensionless time, frequency f is proportional to c_0/R, and the circular frequency w can be expressed in terms of frequency f as follows: $w = 2\pi f$).

3.4. Propagation of rectangular pulses of different durations through an axisymmetric bar

Problems considered in this section differ from those described in Section 3.3, by the shape of a pulse only; i.e., along boundary AB $u_n = v_0\, t$ (which corresponds to the rectangular velocity pulse $v_n = v_0$) and $\tau_n = 0$ for $t \le t_1$, and $\sigma_n = 0$ and $\tau_n = 0$ for $t \ge t_1$ (see Fig. 13). Two long and short durations of the pulse are used in calculations: $t_1 = 20R/c_0$ and $t_2 = 0.1t_1 = 2R/c_0$. The same durations have the sinusoidal pulses of frequencies $f = 0.025c_0/R$ and $f = 0.25c_0/R$ considered in Section 3.3. The numerical results shown below are calculated for a fine mesh with $40 \times 2000 = 80\,000$ (648 162 degrees of freedom) quadratic 9-node elements. Similar to Section 3.3, the new explicit fourth-order TCG method (see [41]) with uniform time increments $\Delta\bar{t} = 0.0004$ is applied for basic computations. At these small time increments, the error in time is small and can be disregarded. At post-processing, the implicit first-order TCG method is applied with 10 uniform time increments (the size of time increments at different observation times is calculated according to Eqs. (A.6)–(A.8)). The comparison of evolution of the velocities in the middle of the external surface of the cylinder for sinusoidal and rectangular pulses is shown in Fig. 14 (for the sinusoidal pulses the results from Figs. 9e and g are used). For the long duration

rectangular pulse, the variation of the axial velocity in time contains a lot of high-frequency oscillations (curve 1 in Fig. 14a) compared to the harmonic pulse of the same duration (curve 2 in Fig. 14a). However, the amplitudes of the high-frequency oscillations of the rectangular pulse in Fig. 14a are much smaller than the amplitude of the initial rectangular pulse. For the short duration rectangular pulse, the variation of the axial velocity in time (curve 1 in Fig. 14b) is very similar to that for the harmonic pulse of the same duration (curve 2 in Fig. 14b). The difference between curves 1 and 2 in Fig. 14b is mainly related to the amplitudes of oscillations. These amplitudes are greater for the rectangular pulse due to the larger input energy of the rectangular pulse. It can be also seen that the duration of the first oscillation in curves 1 and 2 in Fig. 14b is practically the same (see curves 1 and 2 at the time interval between $\bar{t}=20$ and $\bar{t}=30$). It is interesting to mention that the duration of the first oscillation for the long duration rectangular pulse in curve 1 in Fig. 14a is close to that for the short duration rectangular pulse in curves 1 and 2 in Fig. 14b. These observations show that a long cylinder serves as a filter of high-frequency pulses presented in a rectangular pulse (we observed similar behavior of a long cylinder for the propagation of sinusoidal pulses of different frequencies in Section 3.3; see Figs. 9f–h).

3.5. *Propagation of a continuously applied sinusoidal pulse through an axisymmetric bar*

Problems considered in this section differ from those described in Section 3.3, by the duration of a pulse only; i.e., along boundary AB $u_n=v_0[1-\cos(2\pi ft)/(2\pi f)]$ (which corresponds to the sinusoidal velocity pulse $v_n=v_0\sin(2\pi ft)$) and $\tau_n=0$ for

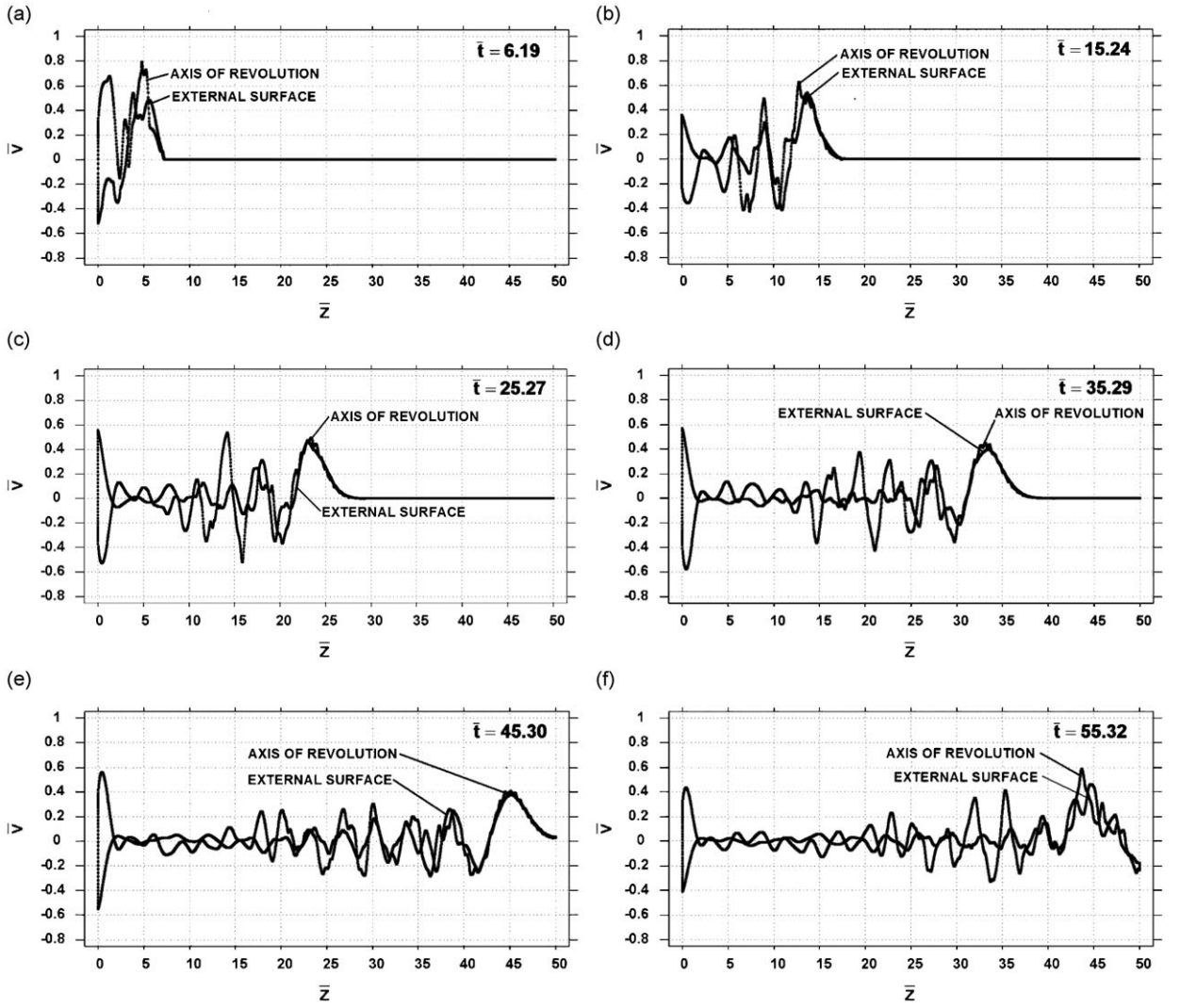

Fig. 11. Distribution of the axial velocity along the axis of revolution and along the axial line on the external surface at different times $\bar{t}=6.19$ (a), 15.24 (b), 25.27 (c), 35.29 (d), 45.30 (e), 55.32 (f), 65.33 (g), 75.34 (h) and 80.35 (i). The sinusoidal velocity pulse of frequency $f=10f_1=0.25c_0/R$ is applied.

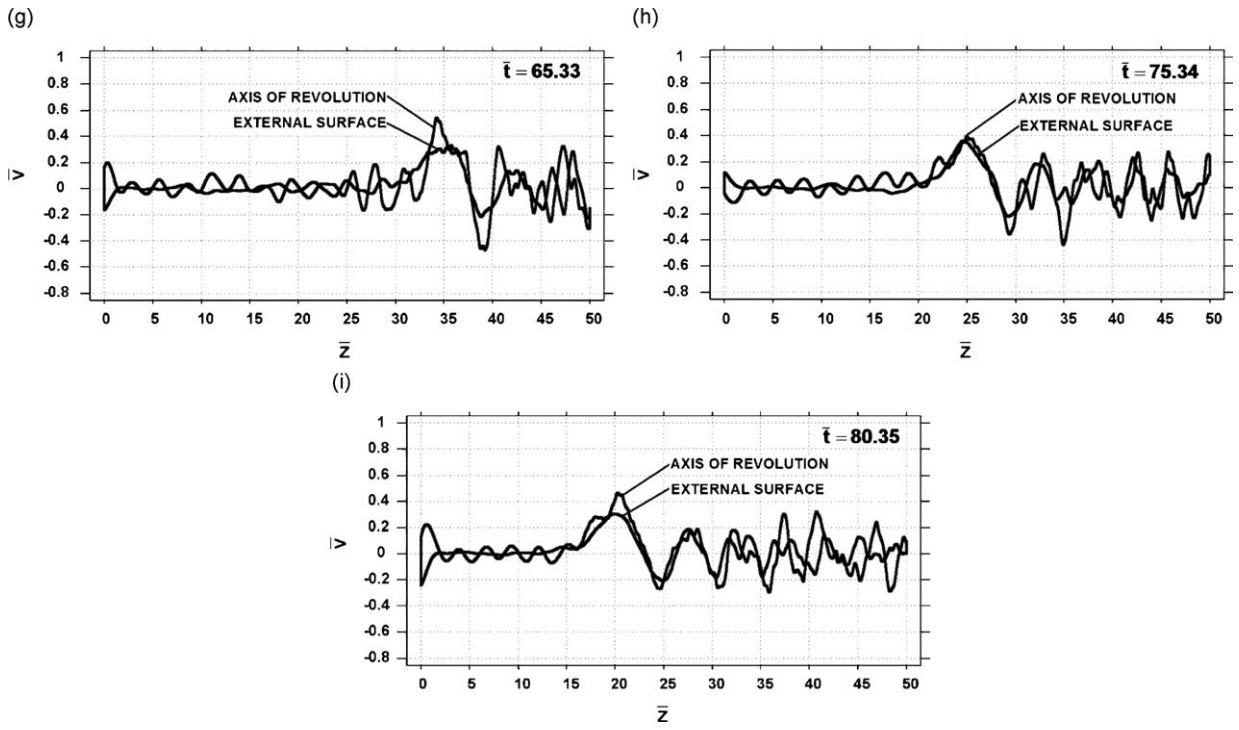

Fig. 11. (*Continued*)

$t \geq 0$; see Fig. 15. It means that a continuously applied sinusoidal excitation of the left end of the cylinder is considered. Because the 1-D theory describes the propagation of low-frequency pulses sufficiently accurately (see Section 3.3 for $f = 0.025c_0/R$), here we will analyze the propagation of a pulse of high frequency $f = 0.25c_0/R$. The numerical results shown below are calculated for a fine mesh with $40 \times 2000 = 80\,000$ (648 162 degrees of freedom) quadratic 9-node elements. Similar to Section 3.3, the new explicit fourth-order TCG method (see [41]) with uniform time increments $\Delta\bar{t} = 0.0004$ is applied for basic computations. At these small time increments, the error in time is small and can be disregarded. At post-processing, the implicit first-order TCG method is applied with 10 uniform time increments (the size of time increments at different observation times is calculated according to Eqs. (A.6)–(A.8)). The distribution of the axial velocity along the axis of revolution and along the axial line on the external surface at different times $\bar{t} = 8$ (a, b), 24 (c, d) and 40 (e, f) is shown in Fig. 16. As can be seen from Fig. 16, the shape of the first oscillation behind the wave front corresponds to low-frequency components (similar to the case of the half-sine pulse in Fig. 11 for the same frequency). This can be explained by the fact that similar to the Pochhammer–Chree solution, low-frequency (high-wavelength) components of the applied pulse propagate with higher velocities. It is also interesting to note that the amplitude of the first oscillation behind the wave front is smaller for the continuously applied pulse (see Fig. 16) than for the half-sine pulse in Fig. 11. The distributions of the axial velocity along the axis of revolution and along the axial line on the external surface at some distance from the wave front are also very different for the continuously applied pulse and the half-sinusoidal pulse. At some distance from the wave front of the continuously applied pulse, the distributions of the axial velocity along the axis of revolution and along the axial line on the external surface resemble a periodic function with a variable amplitude. It is also necessary to emphasize that the uniform sinusoidal excitation of the left end of the bar with the dimensionless velocity amplitude (see Eq. (3)) equal to 1, changes very fast to non-uniform velocity distribution across cross sections even at small distance from the left end (see Fig. 16). The amplitudes of the oscillations in Fig. 16 vary between -1.6 and 1.6 along the axis of revolution and between -0.6 and 0.6 along the external surface.

The obtained numerical results raise the question of whether the traditional dispersion correction that is used in the literature for improving experimental and numerical results for wave propagation in the SHPB ([2–11] and others) is applicable to propagation of high-frequency pulses in a finite cylinder (there is no rigorous mathematical justification of the applicability of the traditional dispersion correction to a finite cylinder with arbitrary boundary and initial conditions). For example, one of the traditional dispersion correction schemes for finite bars is based on the Fourier series expansion of an input pulse applied at one end of a bar and the assumption that each harmonic component of the pulse propagates in a finite bar with a specific constant velocity (determined from the dispersion equation of the Pochhammer–Chree solution) and a constant amplitude; e.g., see [3,4,6]. However, it is not true for high-frequency harmonic pulses propagating in a

finite cylinder; see the numerical results in Fig. 16 (similar numerical results were also obtained for pulses with frequencies $f > 10f_1 = 0.25c_0/R$). It is necessary to mention that the dispersion equation is derived for propagation of harmonic waves with the special non-homogeneous radial distribution of displacements, velocities, or stresses over cross sections of an infinite cylinder. It seems that the main source of inaccuracy in the application of the traditional dispersion correction to a finite bar is the difference in the end boundary conditions for infinite and finite cylinders. The traditional dispersion correction used in the literature for the SHPB [2–11] does not take into account a radial distribution of parameters (like displacements, velocities or stresses) over cross sections of a finite cylinder.

4. Concluding remarks

For the first time accurate solutions for propagation of high-frequency pulses through a long circular cylinder are obtained by the application of a new numerical technique based on the finite element method and the new time-integration strategy. The numerical results show the complicated distribution of velocities in space and time for high-frequency pulses that cannot be described with the help of the traditional dispersion correction used in the literature. These results are very important for the understanding of dynamics experiments in the split Hopkinson pressure bar.

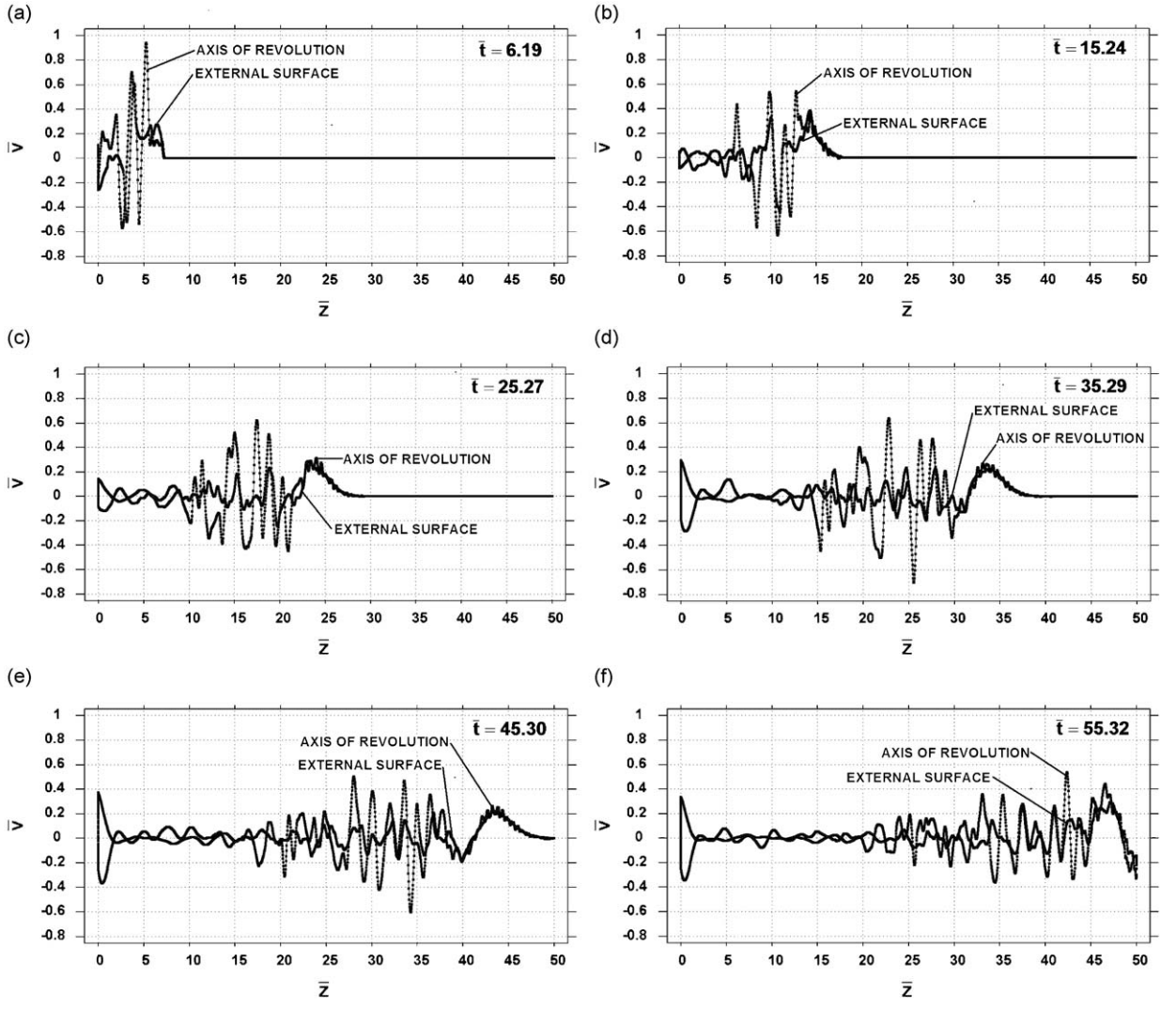

Fig. 12. Distribution of the axial velocity along the axis of revolution and along the axial line on the external surface at different times $\bar{t} = 6.19$ (a), 15.24 (b), 25.27 (c), 35.29 (d), 45.30 (e), 55.32 (f), 65.33 (g), 75.34 (h) and 80.35 (i). The sinusoidal velocity pulse of frequency $f = 20f_1 = 0.5c_0/R$ is applied.

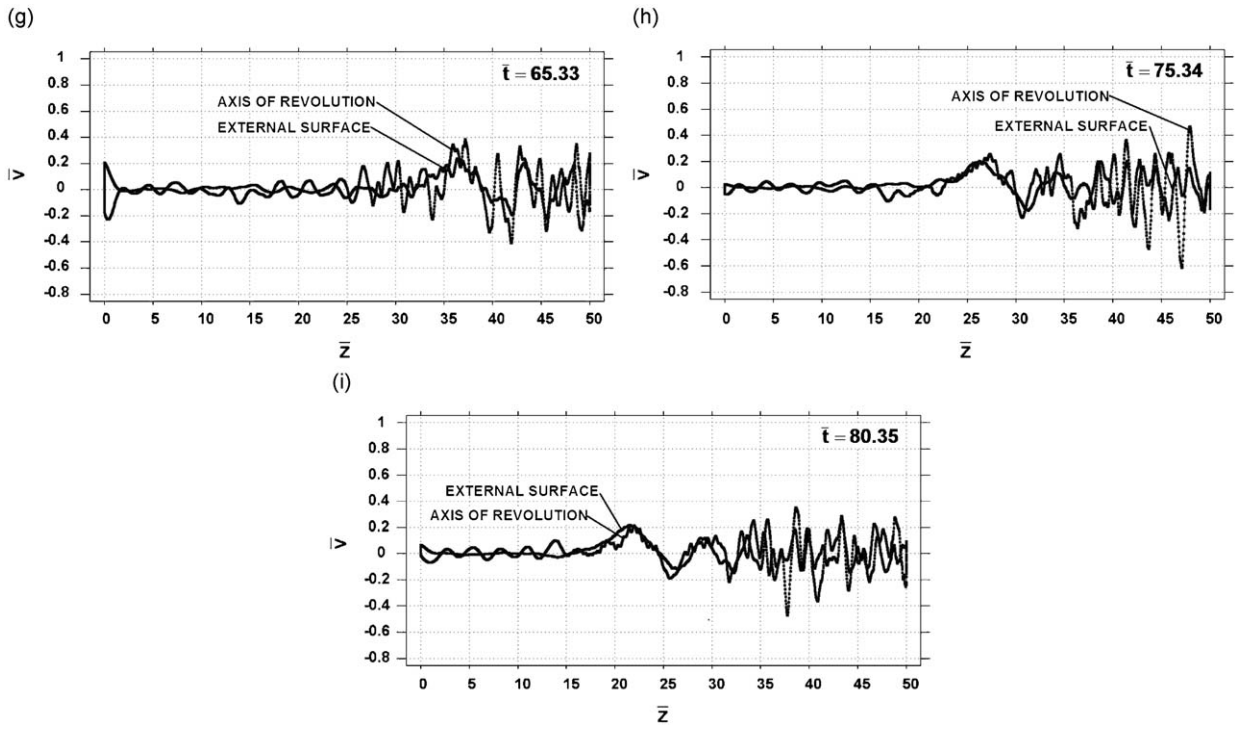

Fig. 12. (*Continued*)

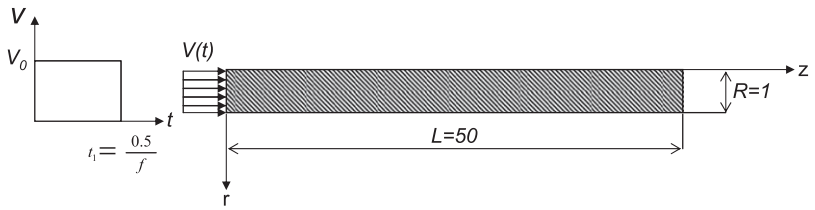

Fig. 13. Propagation of a rectangular pulse along a cylinder. z is the axis of revolution.

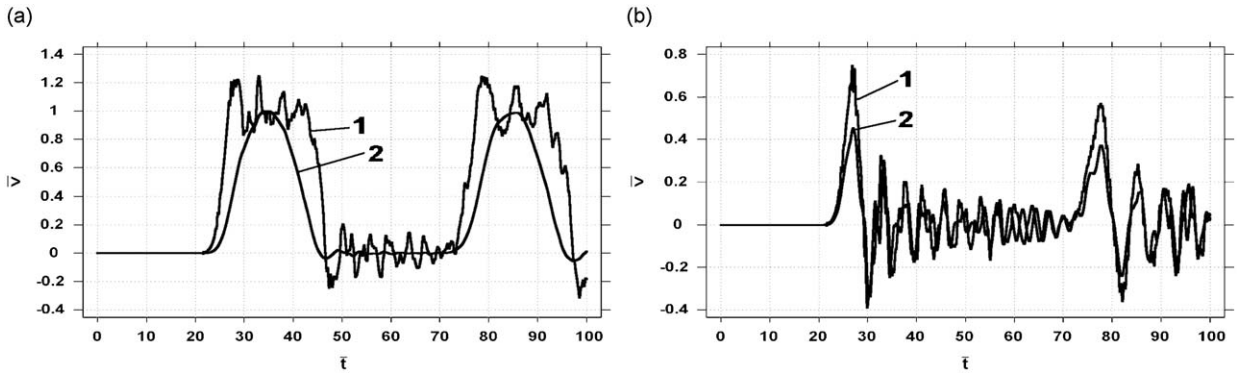

Fig. 14. Variation of the axial velocity in time at the point with the coordinate $z=25$ on the external surface of the cylinder at propagation of rectangular (curves 1) and sinusoidal pulses (curves 2) of duration $t_1 = 20R/c_0$ (a) and $t_2 = 0.1t_1 = 2R/c_0$ (b).

We should also mention that the new finite element technique used in the paper is based on the general form of elastodynamics equations, requires no assumptions used in the analytical approaches (e.g., a possible form of solutions), and can be applied to wave propagation problems with arbitrary boundary and initial conditions. In contrast to standard

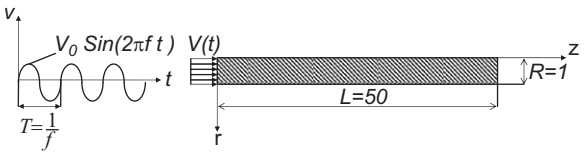

Fig. 15. Propagation of a continuously applied sinusoidal pulse along a cylinder. z is the axis of revolution.

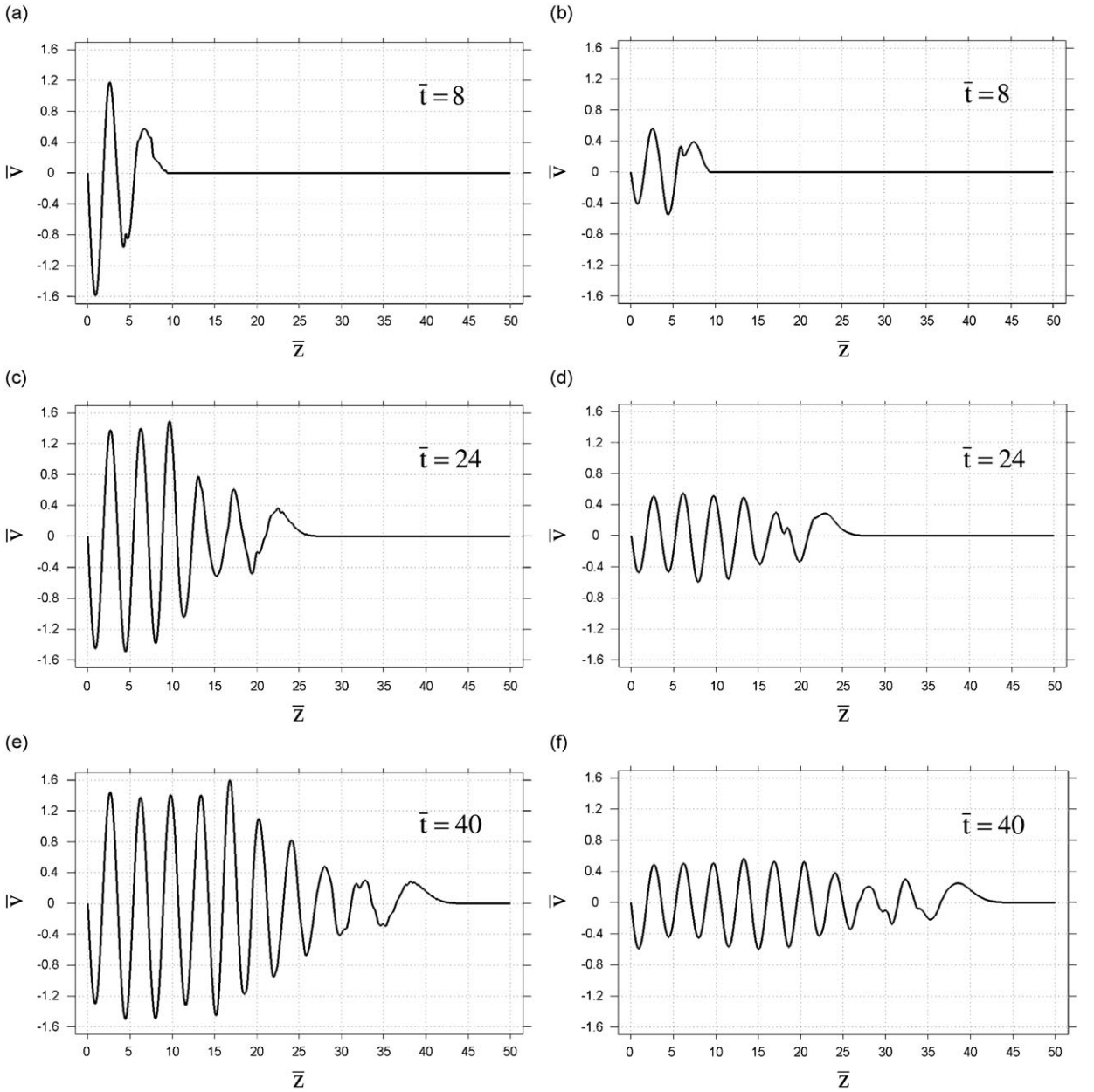

Fig. 16. Distribution of the axial velocity along the axis of revolution (a,c,e) and along the axial line on the external surface (b,d,f) at different instances $\bar{t}=8$ (a,b), 24 (c,d) and 40 (e,f). The continuously applied sinusoidal velocity pulse of frequency $f=10f_1=0.25c_0/R$ is considered.

finite element approaches for elastodynamics, the new technique converges at mesh refinement; i.e., accuracy of the numerical results can be estimated by the use of the mesh refinement (similar to the standard finite element technique for elastostatics). The new technique provides us for the first time the convergence study for propagation of high-frequency pulses through a long circular cylinder.

Acknowledgments

The research of AVI has been supported in part by the Texas Higher Education Coordinating Board under Grant 003644 0008 2006, DOE under Grant DE-FC03-03NA00144, the Air Force Research Lab, Eglin (contract # FA8651-08-D-0108), as well as the support of the Air Force Summer Faculty Fellowship Programs 2007 and 2008. The technical assistance of Himadri Samajder (Texas Tech University) is very much appreciated.

Appendix A. Implicit TCG method for filtering spurious high-frequency oscillations

Let us describe the implicit TCG method with large numerical dissipation suggested in [38,40] that is used for the step-by-step time integration of elastodynamics equations; see Eq. (1). The method is based on the linear approximations of displacements $U(t)$ and velocities $V(t)$ within a time step Δt $(0 \le t \le \Delta t)$

$$\mathbf{U}(t) = \mathbf{U}_0 + \mathbf{U}_1 t, \quad \mathbf{V}(t) = \mathbf{V}_0 + \mathbf{V}_1 t \tag{A.1}$$

and has the first-order of accuracy. Here $\mathbf{U}_0$ and $\mathbf{V}_0$ are the known initial nodal displacements and velocities, and the unknown nodal vector $\mathbf{V}_1$ can be expressed in terms of the unknown nodal vector $\mathbf{U}_1$ as follows:

$$\mathbf{V}_1 = \frac{1}{a_1}\mathbf{U}_1 - \frac{1}{a_1}\mathbf{V}_0. \tag{A.2}$$

Finally, the following system of algebraic equations is solved for the determination of $\mathbf{U}_1$

$$(\mathbf{M} + a_1\mathbf{C} + a_1^2\mathbf{K})\mathbf{U}_1 = -a_1\mathbf{K}\mathbf{U}_0 + \mathbf{M}\mathbf{V}_0 + \mathbf{R}_1, \tag{A.3}$$

where

$$a_1 = \frac{m+2}{m+3}\Delta t, \quad \mathbf{R}_1 = \frac{(m+2)^2}{(m+3)\Delta t^{m+1}}\int_0^{\Delta t} \mathbf{R}(t)t^{m+1}\,\mathrm{d}t. \tag{A.4}$$

The parameter m is responsible for the amount of numerical dissipation. After the calculation of $\mathbf{U}_1$ from Eq. (A.3), the values of displacements and velocities at the end of a time increment Δt are calculated using Eqs. (A.1) and (A.2) for $t = \Delta t$:

$$\mathbf{U}(\Delta t) = \mathbf{U}_0 + \mathbf{U}_1\Delta t, \quad \mathbf{V}(\Delta t) = \mathbf{V}_0 + \mathbf{V}_1\Delta t. \tag{A.5}$$

The spectral radii of the amplification matrix for the implicit TCG method are shown in Fig. 17 for different values of m. The algorithmic damping ratios and the relative period errors are given in Fig. 18. It can been seen from Fig. 17 that the spectral

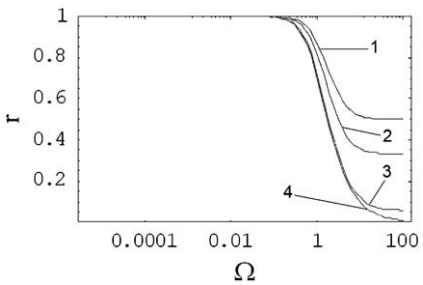

Fig. 17. Spectral radii r for the first-order implicit TCG method with large numerical dissipation. Curves 1, 2, 3, and 4 correspond to $m = 0, 1, 15, \infty$, respectively.

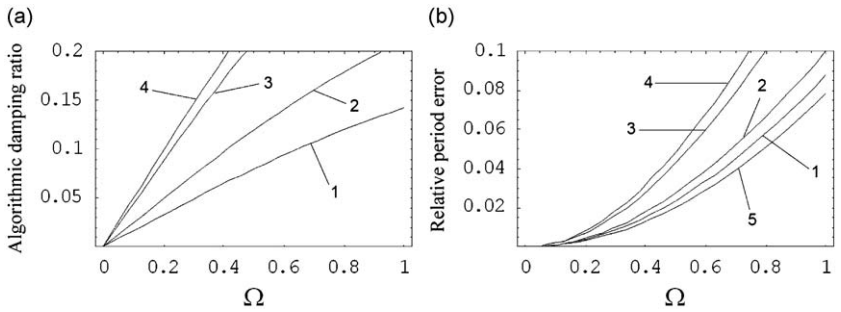

Fig. 18. Algorithmic damping ratios and relative period errors for the first-order implicit TCG method with large numerical dissipation. Curves 1, 2, 3, 4, and 5 correspond to $m = 0, 1, 15, \infty$ and the trapezoidal rule, respectively.

radius decreases (numerical dissipation increases) with the increase in the parameter m. The maximum numerical dissipation corresponds to $m=\infty$. For the case $m=\infty$, the parameter $a_1=\Delta t$, and $\mathbf{R}_1$ should be calculated analytically; see Eqs. (A.4). If the analytical calculation of $\mathbf{R}_1$ at $m=\infty$ is impossible, then a value $m\geq 15$ can be used, because the difference in numerical dissipation for $m=\infty$ and $m\geq 15$ is not very essential (m=15 is used in the current computations). The numerical examples show that the first-order accurate implicit TCG method allows the suppression of spurious high-frequency oscillations for 10 time steps while retaining good accuracy of the solution at low modes. $\mathbf{C}=\mathbf{0}$ (no viscosity) is used in the current computations.

The following empirical formula for the selection of time increments for a time-integration method with large numerical dissipation is suggested in [38,40] for 1-D elastodynamics problems:

$$\Delta t=\alpha(N_1)\frac{\Delta x\Omega_{0.1}(N)}{c}, \tag{A.6}$$

where $c=\sqrt{E/\rho}$ is the wave velocity; Δx is the size of a finite element; $\Omega_{0.1}(N)$ is the value of $\Omega=w\Delta t$ at which the spectral radius has the value 0.1 for the selected number N of time increments; w is the frequency of vibration of the semidiscrete system of finite element Eqs. (1); $\Omega_{0.1}$ is used to scale spectral radii calculated at different numbers of time increments N; $\alpha(N_1)$ is the empirical coefficient depending on the time-integration method, the order of finite elements, and on the number N_1 of elements which are passed through by the wave front (this number can be expressed as $N_1=cT/\Delta x$). For example, for the first-order implicit TCG method (a=0 and m=15), the following explicit expression is suggested in [38] for the coefficient $\alpha(N_1)$:

$$\alpha\left(\frac{cT}{\Delta x}\right)=a_1\left(\frac{cT}{\Delta x}\right)^{a_2}, \tag{A.7}$$

where a_1 = 0.2655 and a_2 = 0.3306 for linear elements, and a_1 = 0.1785 and a_2 =0.2357 for quadratic elements (parameter $\Omega_{0.1}=0.81$ for 10 time increments).

Remark 1. The use of Eqs. (A.6) and (A.7) for different elastodynamics problems is based on the assumption that for different problems the range of spurious high-frequency oscillations depends on the size of finite elements Δx and the observation time T. The numerical dissipation described by Eqs. (A.6) and (A.7) and calibrated for the 1-D impact problem (see the description of the calibration procedure in [38]), indirectly determines and filters all spurious high-frequency oscillations for the given size of a finite element Δx and the given observation time T (uniform meshes in space are assumed). For the 1-D impact problem, all frequencies of a semi-discrete finite element model are excited. For other elastodynamics problems, for which just some frequencies of a semi-discrete model are excited, the numerical dissipation described by Eqs. (A.6) and (A.7) filters the same range of high frequencies as that for the 1-D impact problem. Our experience shows that non-oscillatory numerical results are obtained with Eqs. (A.6) and (A.7) for different elastodynamics problems; i.e., the assumption that the range of spurious oscillations depends on Δx and T, is valid.

Remark 2. For the selection of the size of time increments for post-processing 2-D and 3-D problems, the following modification of Eq. (A.6) can be used:

$$\Delta t=\max_{i,j}\left[\alpha\left(\frac{c_iT}{\Delta x_j}\right)\right]\max_{i,j}\left[\frac{\Delta x_j}{c_i}\right]\Omega_{0.1}(N)=a_1\left[\frac{\max_i(c_i)T}{\min_j(\Delta x_j)}\right]^{a_2}\frac{\max_j(\Delta x_j)}{\min_i(c_i)}\Omega_{0.1}(N), \tag{A.8}$$

where $\max_i(c_i)=\max(c_1,c_2)$ and $\min_i(c_i)=\min(c_1,c_2)$ (i=1,2) are the maximum and minimum values between the velocities of the longitudinal wave c_1 and the transversal wave $c_2=\sqrt{E/(2\rho(1+\nu))}$, Δx_j are the dimensions of finite elements along the axes x_j (j=1,2 for the 2-D problems and j=1,2,3 for the 3-D problems). Eq. (A.8) is based on Eq. (A.6) with the selection of the maximum size of a time increment with respect to the longitudinal and transversal waves, and with respect to the dimensions of a finite element along the coordinate axes. For 2-D and 3-D uniform meshes with linear and quadratic quadrilateral elements in the case of multidimensional problems, we use the coefficients a_1 and a_2 obtained for the 1-D case; see Eq. (A.7).

References

[1] H. Kolsky, *Stress Waves in Solids*, Dover, New York, 1963.
[2] D. Bancroft, The velocity of longitudinal waves in cylindrical bars, *The American Physical Society* 59 (7) (1941) 588–593.
[3] R.M. Davies, A critical study of the Hopkinson pressure bar, *Philosophical Transactions of the Royal Society of London. Series A, Mathematical and Physical Sciences* 240 (821) (1948) 375–457.
[4] J.C. Gong, L.E. Malvern, D.A. Jenkins, Dispersion investigation in the split Hopkinson pressure bar, *Journal of Engineering Materials and Technology, Transactions of the ASME* 112 (3) (1990) 309–314.
[5] J. Lifshitz, H. Leber, Data processing in the split Hopkinson pressure bar tests, *International Journal of Impact Engineering* 15 (6) (1994) 723–733.
[6] P.S. Follansbee, C. Frantz, Wave propagation in the split Hopkinson pressure bar, *Journal of Engineering Materials and Technology, Transactions of the ASME* 105 (1) (1983) 61–66.
[7] R. Guruswami, S. Ghatuparthi, Critical appraisal of limiting strain rates for compression testing of ceramics in a split Hopkinson pressure bar, *Journal of the American Ceramic Society* 77 (1) (1994) 263–267.
[8] C.K.B. Lee, R.C. Crawford, K.A. Mann, P. Coleman, C. Petersen, Evidence of higher Pochhammer–Chree modes in an unsplit Hopkinson bar, *Measurement Science and Technology* 6 (7) (1995) 459–853.

[9] H. Zhao, G. Gary, On the use of SHPB techniques to determine the dynamic behavior of materials in the range of small strains, *International Journal of Solids and Structures* 33 (23) (1996) 3363–3375.
[10] Z. Li, J. Lambros, Determination of the dynamic response of brittle composites by the use of the split Hopkinson pressure bar, *Composites Science and Technology* 59 (7) (1999) 1097–1107.
[11] J.R. Klepaczko, A. Brara, An experimental method for dynamic tensile testing of concrete by spalling, *International Journal of Impact Engineering* 25 (4) (2001) 387–409.
[12] M.-N. Bussac, P. Collet, G. Gary, R. Othman, An optimisation method for separating and rebuilding one-dimensional dispersive waves from multi-point measurements. Application to elastic or viscoelastic bars, *Journal of the Mechanics and Physics of Solids* 50 (2) (2002) 321–349.
[13] P.J. Zhao, T.S. Lok, A new method for separating longitudinal waves in a large diameter Hopkinson bar, *Journal of Sound and Vibration* 257 (1) (2002) 119–130.
[14] R. Skalak, Longitudinal impact of a semi-infinite circular elastic bar, *Journal on Applied Mechanics* 24 (1957) 59–64.
[15] R. Folk, G. Fox, C. Shook, C. Curtis, Elastic strain produced by sudden application of pressure to one end of a cylindrical bar. I. Theory, *Journal of the Acoustical Society of America* 30 (1958) 552–558.
[16] O. Jones, F. Norwood, Axially symmetric cross-sectional strain and stress distributions in suddenly loaded cylindrical elastic bars, *Journal on Applied Mechanics* 34 (1967) 718–724.
[17] L. Kennedy, O. Jones, Longitudinal wave propagation in a circular bar loaded suddenly by a radially distributed end stress, *Journal on Applied Mechanics* 36 (1969) 470–478.
[18] G. Sinclair, J. Miklowitz, Two nonmixed symmetric end-loadings of an elastic waveguide, *International Journal of Solids and Structures* 11 (3) (1975) 275–294.
[19] Y.Y. Kim, C.R. Steele, Effects of lateral surface conditions in time-harmonic nonsymmetric wave propagation in a cylinder, *Journal of Applied Mechanics, Transactions ASME* 56 (4) (1989) 910–917.
[20] I.S. Goldberg, R.T. Folk, Solutions to time-dependent pure-end-condition problems of elasticity: pressure-step wave propagation and end-resonance effects, *SIAM Journal on Applied Mathematics* 53 (5) (1993) 1264–1292.
[21] F. Vales, S. Moravka, R. Brepta, J. Cerv, Wave propagation in a thick cylindrical bar due to longitudinal impact, *JSME International Journal, Series A* 39 (1) (1996) 60–70.
[22] L.D. Bertholf, C.H. Karnes, Two-dimensional analysis of the split Hopkinson pressure bar system, *Journal of the Mechanics and Physics of Solids* 23 (1) (1975) 1–19.
[23] K. Liu, K. Zhao, Z. Gao, T. Yu, Dynamic behavior of ring systems subjected to pulse loading, *International Journal of Impact Engineering* 31 (10) (2005) 1209–1222.
[24] H. Meng, Q. Li, An SHPB set-up with reduced time-shift and pressure bar length, *International Journal of Impact Engineering* 28 (6) (2003) 677–696.
[25] A. Tyas, A.J. Waston, An investigation of frequency domain dispersion correction of pressure bar signals, *Measurement Science & Technology* 11 (2000) 1539–1551.
[26] A. Tyas, A.J. Waston, An investigation of frequency domain dispersion correction of pressure bar signals, *International Journal of Impact Engineering* 25 (2001) 87–101.
[27] R. Govender, T. Cloete, G. Nurick, A numerical investigation of dispersion in Hopkinson pressure bar experiments, *Journal de Physique IV* 134 (2006) 521–526.
[28] B. Karp, A. Dorogoy, Z. Wang, Non-uniform impact excitation of a cylindrical bar, *Journal of Sound and Vibration* 323 (3–5) (2009) 757–771.
[29] H.M. Hilber, T.J.R. Hughes, Collocation, dissipation and 'overshoot' for time integration schemes in structural dynamics, *Earthquake Engineering and Structural Dynamics* 6 (1978) 99–118.
[30] H.M. Hilber, T.J.R. Hughes, R.L. Taylor, Improved numerical dissipation for time integration algorithms in structural dynamics, *Earthquake Engineering and Structural Dynamics* 5 (1977) 283–292.
[31] J.C. Houbolt, A recurrence matrix solution for the dynamic response of elastic aircraft, *Journal of Aeronautical Sciences* 17 (1950) 540–550.
[32] N.M. Newmark, A method of computation for structural dynamics, *Journal of Engineering Mechanics Division of ASCE* 8 (1959) 67–94.
[33] K.C. Park, Evaluating time integration methods for nonlinear dynamic analysis, T. Belytschko et al.(Ed.), *Finite Element Analysis of Transient Nonlinear Behavior, AMD*, vol. 14, ASME, New York, 1975, pp. 35–58.
[34] E.L. Wilson, I. Farhoomand, K.J. Bathe, Nonlinear dynamic analysis of complex structures, *Earthquake Engineering and Structural Dynamics* 1 (1973) 242–252.
[35] O.C. Zienkiewicz, R.L. Taylor, *The Finite Element Method*, Butterworth-Heinemann, Oxford, UK, 2000.
[36] G.M. Zhang, R.C. Batra, Wave propagation in functionally graded materials by modified smoothed particle hydrodynamics (msph) method, *Journal of Computational Physics* 222 (2007) 374–390.
[37] A.V. Idesman, A new high-order accurate continuous Galerkin method for linear elastodynamics problems, *Computational Mechanics* 40 (2007) 261–279.
[38] A.V. Idesman, H. Samajder, E. Aulisa, P. Seshaiyer, Benchmark problems for wave propagation in elastic materials, *Computational Mechanics* 43 (6) (2009) 797–814.
[39] A.V. Idesman, Solution of linear elastodynamics problems with space-time finite elements on structured and unstructured meshes, *Computer Methods in Applied Mechanics and Engineering* 196 (2007) 1787–1815.
[40] A.V. Idesman, A new solution strategy and a new look at selection of time-integration methods for linear elastodynamics, *International Journal for Numerical Methods in Engineering* (2009) 1–40, under review.
[41] A.V. Idesman, M. Schmidt, R.L. Sierakowski, A new explicit predictor-multicorrector high-order accurate method for linear elastodynamics, *Journal of Sound and Vibration* 310 (2008) 217–229.
[42] T.J.R. Hughes, *The Finite Element Method: Linear Static and Dynamic Finite Element analysis*, Prentice-Hall, Englewood Cliffs, NJ, 1987.
[43] K.J. Bathe, *Finite Element Procedures*, Prentice-Hall, Upper Saddle River, New Jersey, 1996.
[44] G.M. Hulbert, Discontinuity-capturing operators for elastodynamics, *Computer Methods in Applied Mechanics and Engineering* 96 (3) (1992) 409–426.
[45] G.M. Hulbert, T.J.R. Hughes, Space-time finite element methods for second-order hyperbolic equations, *Computer Methods in Applied Mechanics and Engineering* 84 (3) (1990) 327–348.
[46] L. Jiang, R.J. Rogers, Effects of spatial discretization on dispersion and spurious oscillations in elastic wave propagation, *International Journal for Numerical Methods in Engineering* 29 (6) (1990) 1205–1218.
[47] J.D. Achenbach, *Wave Propagation in Elastic Solids*, North-Holland, American Elsevier Pub. Co., Amsterdam, New York, 1973.